Screened potential in one-dimensional systems: Application to electron-hole interaction and Wannier-Mott-like excitons in atomic wires

F. Bechstedt,[1] S. Grillo,[2,3] O. Pulci,[2] and P. Gori[4]

[1]*Institut für Festkörpertheorie und -optik, Friedrich-Schiller-Universität Jena, Max-Wien-Platz 1, 07743 Jena, Germany*
[2]*Department of Physics and INFN, University of Rome Tor Vergata, Via della Ricerca Scientifica 1, 00133 Rome, Italy*
[3]*Max Planck Institute for the Structure and Dynamics of Matter and Center for Free-Electron Laser Science, Hamburg 22761, Germany*
[4]*Department of Industrial, Electronic and Mechanical Engineering, Roma Tre University, Via della Vasca Navale 79, 00146 Rome, Italy*

(Received 15 December 2025; revised 26 May 2026; accepted 15 June 2026; published 29 June 2026; corrected 11 August 2026)

The geometry and electronic properties of nanostructures such as chains, wires, and ribbons, which are restricted in two dimensions, give rise to novel and unexpected physical phenomena. We derive the screened Coulomb potential in one-dimensional (1D) systems by solving the Poisson equation for different spatial distributions of the responding electron gas across the cross section, characterized by a 1D static electronic polarizability α_{1D}. Both local and nonlocal screening responses are examined. Starting from three different bare soft-core or truncated potentials of the 1D hydrogen atom, we construct seven corresponding models for the screened interaction. These screened model potentials are then applied to describe exciton binding energies using a variational approach with a trial function based on the ground-state wave function of the 1D hydrogen atom. We explicitly study atomic wires composed of MgN_2, S_3, Te_3, As_2S_3, and Bi_2Te_3. The required parameters, including wire geometry, static electronic polarizability, and effective electron and hole masses, are computed within density functional theory. We find that reduced screening at short distances and antiscreening at longer distances lead to extraordinarily large exciton binding energies in the range of 1-4 eV. For extremely thin atomic wires, binding energies even larger than the values without screening are predicted. The exciton binding energy E_B and radius r_B obtained from the variational treatment are compared with *ab initio* results from many-body perturbation theory using the *GW* approximation and solutions of the Bethe–Salpeter equation. Chemical trends are traced back to material parameters such as electronic polarizability and effective interband masses. From the comparison with the first-principles results, we identify the most accurate screening model for 1D systems.

DOI: 10.1103/56y9-s71s

I. INTRODUCTION

Quasi-one-dimensional (1D) materials have attracted considerable interest not only from the viewpoint of fundamental physics but also because of their potential applications in electronic, optoelectronic, and optical devices. They represent systems in which electrons and holes are free to move predominantly along a single spatial direction. Due to the accompanying quantum confinement in the two perpendicular directions, one of the most striking features of 1D systems is the inverse-square-root divergence of the single-particle density of states (DOS), as well as of the two-particle joint density of states (JDOS). While the DOS strongly influences the electronic properties, the electron-hole JDOS drastically modifies optical interband transitions through the analog of the van Hove singularities in optical spectra. The redistribution of the DOS also significantly affects the interaction between excited electrons and holes and, consequently, the excitonic effects in emission and absorption spectra. In semiconducting arrangements, 1D excitons are formed by a long-range but screened Coulomb interaction between electron and hole. The screening is governed by the electronic polarization of the 1D system and its surrounding environment. In the freestanding case, where external screening is negligible, the Coulomb interaction becomes enhanced and strong exciton binding energies are expected.

There exist several classes of quasi-1D systems. One realization is provided by quantum wires fabricated from inorganic semiconductors, where quasi-1D semiconductor pieces with smaller gaps are embedded within wider-gap semiconductor materials [1]. These structures exhibit pronounced optical anisotropy and stimulated emission [2,3]. In such quasi-1D heterostructures, excitonic effects play a particularly important role due to the confinement in two transverse directions. Strongly bound excitons are formed through the screened Coulomb attraction between electron and hole along the wire axis [4,5]. Similar systems are freestanding semiconductor quantum wires with diameters on the order of the de Broglie wavelength of the electrons. Such wires can be prepared through several recently developed techniques, including direct growth on suitable substrates [6–8], synthesis assisted by molecular directing agents [9,10], and encapsulation inside single-walled carbon nanotubes [11]. An especially promising approach for accessing isolated quasi-1D wires is

Published by the American Physical Society under the terms of the Creative Commons Attribution 4.0 International license. Further distribution of this work must maintain attribution to the author(s) and the published article's title, journal citation, and DOI.

the exfoliation of strongly anisotropic three-dimensional (3D) crystals composed of covalently bonded inorganic chains. In these materials, individual 1D wires are arranged in a crystal lattice via weak inter-chain van der Waals interaction, enabling their separation through mechanical or chemical exfoliation techniques [12–17], in close analogy to exfoliation methods used for two-dimensional (2D) materials. Moreover, atomic chains deposited on semiconducting substrates may serve as structural elements for optoelectronic applications when a fundamental band gap is opened [18]. Such systems can exhibit pronounced Coulomb interaction effects [19].

Another important class of quasi-1D systems is based on carbon arrangements, with carbon nanotubes representing the most prominent example [20]. In particular, semiconducting single-walled nanotubes exhibit exciton binding energies reaching values of about 1 eV [21–23]. Atomically thin 2D semiconductors, such as graphene subjected to confinement in one spatial direction, provide further model systems. For instance, graphene nanoribbons support excitons with binding energies up to 0.7 eV [24,25] and biexcitons with binding energies around 250 meV [26]. The ideal 1D limit is even more closely realized in atomic chains. Prototypical examples include monoatomic chains of *sp*-hybridized carbon atoms, known as carbynes [27], and carbon chains with alternating single and triple bonds, commonly referred to as polynes [28]. In the hydrogenated case, chains exhibiting alternating weak and strong bonds—reminiscent of polyacetylene—have been shown to display pronounced excitonic effects [29,30].

Recently, other chain structures that do not exhibit the characteristic single, double or triple bonds of carbon atoms have been investigated for their strong many-body effects and optical properties. Among them are single-helical chains of trigonal Te atoms [31–33]. More complex chainlike structures with partial ionic character have also been explored in 1D compounds with various stoichiometries. Prominent examples are metal chalcogenide wires [34–37]. Giant exciton binding energies of about 1.6 eV have been predicted for Mo_6Te_6 and W_6Te_8 atomic wires. However, due to their narrow gaps, exciton instability and the possible formation of excitonic-insulator states have been discussed [37]. Similar excitonic instabilities have also been predicted for all-metal nanowires [38]. In addition to the trigonal Te chains composed of Te_3 units, sulfur-based wires S_3 have been examined alongside related compounds such as Bi_2Te_3 and As_2S_3 [33].

Quasiparticle and excitonic effects can be investigated from first principles within many-body perturbation theory (MBPT) [39]. Independent of the system dimensionality, the excitation processes following the optical generation of electron-hole pairs are treated using Hedin's *GW* approximation (*G*: single-particle Green's function; *W*: screened Coulomb interaction) for the single-particle exchange-correlation (XC) self-energy. The corresponding two-particle effects, mediated by the electron-hole interaction, are then described by solving the Bethe-Salpeter equation (BSE). The *ab initio* implementation of MBPT is available in several numerical packages, most notably the YAMBO code [40]. Typically, the starting atomic geometries are optimized within density functional theory (DFT) [41], while the underlying electronic structure is obtained from the Kohn-Sham (KS) scheme [42] using an appropriate XC functional. The corresponding numerical treatments are implemented, for instance, in the QUANTUM ESPRESSO suite [43,44]. These MBPT and DFT approaches can be applied equally well to nanostructures with confinement in one, two, or even three spatial directions, using supercell techniques and a suitable handling of the long-range Coulomb interaction [45–47].

Excitonic effects can also be treated in a more analytical manner [39]. Within the effective-mass approximation (EMA) [48], the kinetic energies of electrons and holes are described by parabolic bands, while their mutual attraction is modeled by a statically screened potential W characterized by an effective dielectric constant. Under these assumptions, analytical expressions can be derived for the pair excitation energies and wave functions, as well as for the optical absorption near the fundamental gap [39]. For 2D quantum-well systems, more sophisticated analytical forms of the screened potential have been developed [49,50], to incorporate environmental screening. These expressions were later refined to include screening within the 2D material itself through a static electronic polarizability [51–53]. In the 1D case, however, an equally efficient analytical description of screening originating from the electronic system—characterized by a static polarizability α_{1D}—is still largely lacking.

In this work, we propose models to describe the static dielectric response of quasi-1D systems characterized by the static electronic polarizability α_{1D}. Beyond providing physical insight, these analytical models offer a computationally inexpensive alternative to full GW + BSE calculations. Using classical electrostatics within a continuum framework, we derive several expressions for the screened potential W in Sec. II. These expressions differ in the assumptions made about how the screening charge redistributes over the wire cross section and about the degree of nonlocality in the interaction between the excited charges and the screening electron gas. The resulting forms of W are then combined with the EMA.

To obtain an almost analytical model for the exciton binding energy, we employ a variational approach in Sec. III, using as a trial function the ground-state orbital of the 1D hydrogen atom. The required input parameters—geometrical characteristics of the wire cross section, the static electronic polarizability, and the effective masses—are extracted from *ab initio* calculations for atomic chains composed of S_3, Te_3, As_2S_3, Bi_2Te_3, and MgN_2, as discussed in Sec. IV. For the same 1D systems, we also report the exciton binding energies and localization radii of the lowest electron–hole excitations computed within the BSE + GW framework. In the discussion section (Sec. V), the binding energies and radii predicted by our analytical model are compared with the *ab initio* results, allowing us to evaluate and validate the proposed screening models. Finally, Sec. VI provides a summary and concluding remarks.

II. STATICALLY SCREENED COULOMB POTENTIAL IN QUASI-1D SYSTEMS

A. Electrostatic treatment

In deriving the screened potential of a quasi-1D system, whose screening response is characterized by its static electronic polarizability α_{1D} within the electrostatic continuum

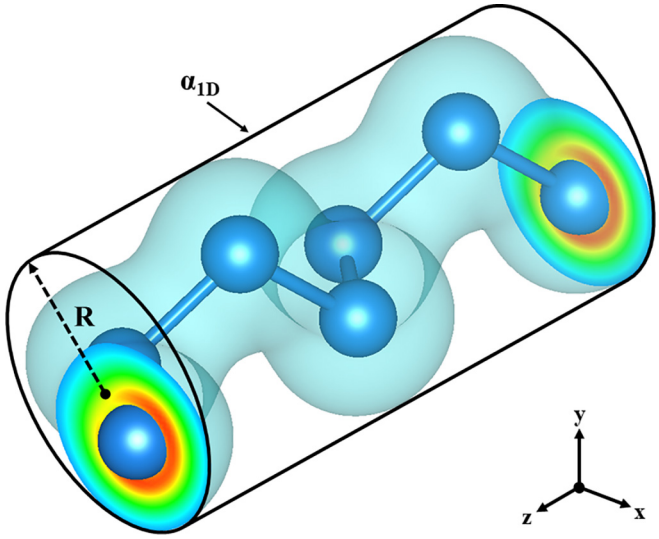


FIG. 1. Illustration of the electrostatic problem for a quasi-1D system, modeled by a cylindrical region embedding the real atomic chain oriented along the z direction. As an example, an S_3 chain is shown (S atoms and S-S bonds in dark blue). The spatial extent of the electronic states is indicated by the electronic charge density (light blue). The resulting electrostatic model is represented by a cylinder with characteristic cross-sectional radius R. The screening response of the electronic system is described by the static polarizability α_{1D}.

theory, we follow the conceptual framework established for two-dimensional systems [51–53], which leads to the Rytova-Keldysh potential for quantum wells [49,50]. In that case, the 2D electronic polarizability α_{2D} is related to the static electronic dielectric constant ϵ_∞ and the material thickness d via $\alpha_{2D} = d(\epsilon_\infty - 1)/4\pi$. In general, the electrostatic potential $\varphi(\mathbf{r})$ generated by a charge distribution in a polarizable medium embedded in vacuum is governed by the Poisson equation [54]

$$\Delta_{\mathbf{r}}\varphi(\mathbf{r}) = -4\pi[n_{\text{ext}}(\mathbf{r}) + n_{\text{ind}}(\mathbf{r})], \tag{1}$$

with the external charge density $n_{\text{ext}}(\mathbf{r}) = e\delta(\mathbf{r})$ corresponding to a point charge placed at the coordinate origin $\mathbf{r} = 0$.

To model the quasi-1D system, we consider an electronic structure of cylindrical symmetry oriented along the z axis, with a finite cross section in the xy plane. The cross section may be rectangular or circular, with total area A (see Fig. 1). In this geometry, the induced charge density $n_{\text{ind}}(\mathbf{r})$ describes the screening response of the electrons confined within this finite cross-sectional region.

Since the z component of the polarization field is proportional to the corresponding electric field $-\frac{d}{dz}\varphi(\boldsymbol{\rho}, z)$ with $\boldsymbol{\rho} = (x, y)$, the induced charge in (1) can be written as

$$n_{\text{ind}}(\boldsymbol{\rho}, z) = \alpha_{1D} f(\boldsymbol{\rho}) \frac{d^2}{dz^2}\varphi(\boldsymbol{\rho}, z). \tag{2}$$

Here the function $f(\boldsymbol{\rho}) = f(x, y)$ describes the spatial distribution of the induced charge within the cross section of the wire, normalized per unit area. This function provides an approximate characterization of the region in which the electronic states responsible for screening are localized, as well as the region where the direct Coulomb interaction between charged particles is effective. In Eq. (2), the overall strength of the screening response of the quasi-1D electronic system is encoded in the static polarizability α_{1D} (see also Fig. 1). The approach for the induced charge in (2) follows the idea of modern derivations [53,55] of the Rytova-Keldysh potential, as $\alpha_{2D} f(z)\, \Delta_{\boldsymbol{\rho}}\varphi(\boldsymbol{\rho}, z)$, with the 2D Laplace operator $\Delta_{\boldsymbol{\rho}}$ and the distribution function $f(z)$ over the sheet thickness. Indeed, for infinitely thin layers with $f(z) = \delta(z)$, the solution of the Poisson equation (1) yields the 2D Rytova–Keldysh potential, but with a static 2D polarizability α_{2D} rather than a dielectric constant ϵ_∞ of the underlying bulk material forming the thin layer.

The symmetry of the quasi-1D system suggests the use of 3D Fourier transformations, with a 3D wave vector $(\mathbf{Q}, q)$, where $\mathbf{Q} = (Q_x, Q_y)$, defined as

$$\varphi(\boldsymbol{\rho}, z) = \frac{1}{(2\pi)^3}\int d^2\mathbf{Q}\int_{-\infty}^{+\infty} dq\, \tilde{\varphi}(\mathbf{Q}, q) e^{i[\mathbf{Q}\cdot\boldsymbol{\rho} + qz]},$$
$$\tilde{\varphi}(\mathbf{Q}, q) = \int d^2\boldsymbol{\rho}\int_{-\infty}^{+\infty} dz\, \varphi(\boldsymbol{\rho}, z) e^{-i[\mathbf{Q}\cdot\boldsymbol{\rho} + qz]}. \tag{3}$$

Using the external charge density $n_{\text{ext}}(\mathbf{r})$ and the induced charge density $n_{\text{ind}}(\mathbf{r})$ from Eq. (2), the Poisson equation (1) transforms into

$$(Q^2 + q^2)\,\tilde{\varphi}(\mathbf{Q}, q) = 4\pi e - 4\pi\alpha_{1D} q^2 \times \int d^2\boldsymbol{\rho}\, f(\boldsymbol{\rho}) e^{-i\mathbf{Q}\cdot\boldsymbol{\rho}} \tilde{\tilde{\varphi}}(\boldsymbol{\rho}, q), \tag{4}$$

with the partially Fourier-transformed screened potential

$$\tilde{\tilde{\varphi}}(\boldsymbol{\rho}, q) = \int_{-\infty}^{+\infty} dz\, \varphi(\boldsymbol{\rho}, z)\, e^{-iqz}. \tag{5}$$

Equation (4) can be formally solved using the Green's function of the inhomogeneous Helmholtz equation in cylindrical coordinates [54]. This Green's function is expressed in terms of the zeroth-order modified Bessel function of the second kind [56,57]:

$$K_0(|q|\rho) = \frac{1}{2\pi}\int d^2\mathbf{Q}\frac{e^{i\mathbf{Q}\cdot\boldsymbol{\rho}}}{Q^2 + q^2}. \tag{6}$$

Using this representation, we obtain the integral equation

$$\tilde{\tilde{\varphi}}(\boldsymbol{\rho}, q) = 2eK_0(|q|\rho) + - 2\alpha_{1D} q^2 \int d^2\boldsymbol{\rho}'\, f(\boldsymbol{\rho}') K_0\big(q|\boldsymbol{\rho} - \boldsymbol{\rho}'|\big)\tilde{\tilde{\varphi}}(\boldsymbol{\rho}', q). \tag{7}$$

Assuming a radially homogeneous wire and performing the angle integration, (7) may be interpreted as a special form of standard Fredholm equation of second kind [58]. Similar equations have been applied to solve the electrostatic problem for a dielectric needle model [59] for polymer chains [60] or the 1D Fermi gas with δ-function interaction [61]. The integral equation (7) for the partially Fourier-transformed screened potential $\tilde{\tilde{\varphi}}(\boldsymbol{\rho}, q)$ can be solved approximately.

We are interested in a 1D screened potential $eV(z)$ that depends only on the longitudinal coordinate z. Such a quantity is obtained by averaging the partially transformed potential

$\tilde{\tilde{\varphi}}(\boldsymbol{\rho}, q)$ over the lateral distribution of the induced charge,

$$e\widetilde{V}(q) = \frac{1}{N_f}\int d^2\boldsymbol{\rho} f(\boldsymbol{\rho})\tilde{\tilde{\varphi}}(\boldsymbol{\rho}, q), \tag{8}$$

with the normalization constant

$$N_f = \int d^2\boldsymbol{\rho} f(\boldsymbol{\rho}). \tag{9}$$

The 1D Fourier transform of Eq. (8) then defines the 1D attractive screened potential energy,

$$W(z) = -e^2\int_{-\infty}^{+\infty}\frac{dq}{2\pi}e^{iqz}\widetilde{V}(|q|), \tag{10}$$

which is an even function, $W(z) = W(-z)$. The averaging procedure in Eq. (8) leads to a modified integral equation for $\widetilde{V}(q)$, which can formally be solved to yield

$$\widetilde{V}(q) = \frac{\widetilde{V}_{\text{bare}}(q)}{1 + \alpha_{1\text{D}}q^2\chi(q)\widetilde{V}_{\text{bare}}(q)}. \tag{11}$$

Here,

$$\widetilde{V}_{\text{bare}}(q) = \frac{2}{N_f}\int d^2\boldsymbol{\rho} f(\boldsymbol{\rho})K_0(|q|\rho) \tag{12}$$

is the averaged bare Coulomb potential, obtained by applying Eq. (8) to Eq. (7) with $\alpha_{1\text{D}} = 0$.

The term

$$\chi(q) = N_f\frac{\int d^2\boldsymbol{\rho} f(\boldsymbol{\rho})\int d^2\boldsymbol{\rho}' f(\boldsymbol{\rho}')K_0(|q||\boldsymbol{\rho} - \boldsymbol{\rho}'|)\tilde{\tilde{\varphi}}(\boldsymbol{\rho}', q)}{\int d^2\boldsymbol{\rho} f(\boldsymbol{\rho})K_0(|q|\rho)\int d^2\boldsymbol{\rho}' f(\boldsymbol{\rho}')\tilde{\tilde{\varphi}}(\boldsymbol{\rho}', q)} \tag{13}$$

is a form factor that accounts for the nonlocality of the screening reaction in the quasi-1D system, as encoded in the lateral charge distribution $f(\boldsymbol{\rho})$.

The calculation of the form factor $\chi(q)$ in Eq. (13) requires specifying the distribution function $f(\boldsymbol{\rho})$. Moreover, $\chi(q)$ depends explicitly on the screened potential $\tilde{\tilde{\varphi}}(\boldsymbol{\rho}, q)$, which is not known *a priori*. For this reason, an approximate treatment of Eq. (13), in particular, of the nonlocal term in the numerator mediated by the Green's function $\sim K_0(q|\boldsymbol{\rho} - \boldsymbol{\rho}'|)$, is generally necessary. An appropriate starting point is the fact that we consider narrow, atomically thin quasi-1D systems, for which the almost vanishing lateral coordinates satisfy $\rho \to 0$ and $\rho' \to 0$, consistent with the localization implied by the distributions $f(\boldsymbol{\rho})$ and $f(\boldsymbol{\rho}')$. This local character of the screening response is further reinforced by the radial decay of the screened potential $\tilde{\tilde{\varphi}}(\boldsymbol{\rho}', q)$ at distances far from the center of the wire cross section. Consequently, $K_0(q|\boldsymbol{\rho} - \boldsymbol{\rho}'|)$ can be expanded in a Taylor series with respect to ρ'. Neglecting the nonlocality, one approximates it by its lowest-order term $K_0(q\rho)$, which appears as a prefactor of the $\boldsymbol{\rho}'$ integral, consistent with the mean value theorem for integrals. Under this assumption, Eq. (13) simplifies considerably and yields

$$\chi(q) = N_f. \tag{14}$$

The approximation of the kernel $K_0(q|\boldsymbol{\rho} - \boldsymbol{\rho}'|)$ leads to the same structure factor as obtained from an approximate treatment of the inhomogeneous term on the right-hand side of the Poisson equation (4). In all studied realizations of quasi-1D systems, the lateral extent of the electronic states becomes vanishingly small. As a consequence, only small values of ρ contribute significantly to the area integral in the inhomogeneity. In this limit, the exponential factor $e^{-i\mathbf{Q}\cdot\boldsymbol{\rho}}$ in Eq. (4) can be approximated by the zeroth-order term of its Taylor expansion, $e^{-i\mathbf{Q}\cdot\boldsymbol{\rho}} \approx 1$. With this replacement, the quantity $\widetilde{V}(q)$ introduced in Eq. (8) governs the inhomogeneous part of the Poisson equation, and the same simplifications used in evaluating Eq. (13) lead directly to the result in Eq. (14). For extreme limits, here for small wire extents, approximations of the integral kernel of the Fredholm equations have also been discussed for the dielectric needle model [60,61]. The nonlocality factor $\chi(q)$ Eq. (13) represents an explicit measure of the influence of the finite wave vectors and, hence, the exponential $e^{-i\mathbf{Q}\cdot\boldsymbol{\rho}}$. Therefore, we study the effect of this factor in detail by the expressions (19), (22), and (25) for (nonlocal) models 3, 5, and 7, respectively, in comparison to the cases $Q = 0$ and $\chi(q) = 1$, i.e., (local) models 2, 4, or 6, on the dielectric functions and the screened potentials. The deviations of $\chi(q)$ from the value $\chi(q) = 1$ are due to the deviations of $e^{-i\mathbf{Q}\cdot\boldsymbol{\rho}}$ from 1.

B. Specification of induced charge distribution

We follow ideas developed for truly 2D systems, where layers are considered infinitely thin and are described by the Rytova–Keldysh potential through a δ-function-like polarization distribution $f(z) = \delta(z)$. The consideration of real 1D systems with the distribution function $f(\boldsymbol{\rho}) = \delta(\boldsymbol{\rho})$ in the kernel of the integral equation (7) is, however, not possible because of the logarithmic singularity in the inhomogeneity $K_0(|q|\rho)$ for vanishing radii $\rho \to 0$. Therefore, more realistic quasi-1D systems have to be studied with finite extents and distribution functions $f(\boldsymbol{\rho})$, which model the distribution over the cross section of the induced charge close to this behavior, determined by the underlying squared modulus of the contributing wave functions. Three main cases are of interest: (i) distribution of induced charge mainly near the surfaces of the 1D object; (ii) almost homogeneous distribution over the cross section, and (iii) maximum of the polarization response occurs in the center of the cross section but is far from a δ-function-like action.

1. Model 1: Surface-induced density of nanoribbon

We describe the quasi-1D system as a nanoribbon with a rectangular cross section, defined by $|x| \leqslant L/2$ and $|y| \leqslant h/2$, where L denotes the ribbon width and h its height. As a first approximation, we assume that the induced charge is effectively localized on the surface of the nanoribbon [25], i.e.,

$$f(x, y) = \delta\left(|x| - \frac{L}{2}\right)\delta\left(|y| - \frac{h}{2}\right), \tag{15}$$

with $N_f = 4$. With this choice of distribution, the averaged bare Coulomb potential in Eq. (12) becomes

$$\widetilde{V}_{\text{bare}}(q) = 2K_0(|q|\sqrt{L^2 + h^2}/2). \tag{16}$$

The symmetric form of the charge distribution (15) implies the symmetry relations

$$\tilde{\tilde{\varphi}}\left(\tfrac{L}{2},\tfrac{h}{2},q\right)=\tilde{\tilde{\varphi}}\left(-\tfrac{L}{2},\tfrac{h}{2},q\right)=\tilde{\tilde{\varphi}}\left(\tfrac{L}{2},-\tfrac{h}{2},q\right)=\tilde{\tilde{\varphi}}\left(-\tfrac{L}{2},-\tfrac{h}{2},q\right).$$

Nevertheless, despite the strongly localized representation of the distribution in Eq. (15), the exact expression (13) for $\chi(q)$ cannot be used. Because of the strong localization, the inhomogeneous term in Eq. (13) produces logarithmic singularities arising from vanishing distances in the argument of the Bessel function K_0. As a consequence, the dielectric function goes to infinity, resulting in a vanishing screened potential. For this reason, we do not further investigate the screening with nonlocal effects. Rather, we adopt the approximate local result $\chi(q)=N_f$ given in Eq. (14). In the limit of extremely flat nanoribbons, $h\to 0$, Eqs. (11) and (16) reduce to the expression recently derived by Villegas and Rocha [25].

2. Models 2 and 3: Surface-induced density of nanorod

We now investigate a cylindrical 1D system (see Fig. 1) with a circular cross section of radius R, where $\rho\leqslant R$. In the limit of vanishing lateral extent, $R\to 0$, we again assume that the induced charge density is effectively localized at the surface of the rod. Accordingly, we choose

$$f(\rho)=\frac{1}{2\pi R}\delta(\rho-R), \tag{17}$$

for which the normalization constant is $N_f=1$. With this distribution, the averaged bare Coulomb potential becomes

$$\widetilde{V}_{\text{bare}}(q)=2K_0(|q|R). \tag{18}$$

Because the distribution function (17) contains a Dirac delta, the form factor (13) can be evaluated analytically. Using the relation (cf. [57], p. 688, 6.567.11)

$$\int_0^{2\pi}\frac{d\varphi}{2\pi}K_0(|q|R\sqrt{2}\sqrt{1-\cos\varphi})=I_0(|q|R)K_0(|q|R),$$

one finds

$$\chi(q)=I_0(|q|R) \tag{19}$$

for the 1D system with cylindrical symmetry, which we refer to as (nonlocal) model 3. Compared with the approximate, purely local solution $\chi(q)=1$ [model 2, Eq. (14)], the deviation of $I_0(|q|R)>1$ from $I_0(0)=1$ for finite wave vectors q reflects the influence of nonlocality in the screening reaction. Nonlocal effects become more pronounced with increasing wave vector q.

3. Models 4 and 5: Homogeneously distributed induced density

We next consider an induced charge density that is homogeneously distributed over the wire cross section,

$$f(\rho)=\frac{1}{\pi R^2}\Theta(R-\rho), \tag{20}$$

with $N_f=1$. The corresponding averaged bare Coulomb potential is derived in Appendix A and reads

$$\widetilde{V}_{\text{bare}}(q)=\left[\frac{1}{|q|R}-K_1(|q|R)\right]\frac{4}{|q|R}, \tag{21}$$

and is ruled by the first-order modified Bessel function of the second kind [56,57].

In addition to the description of the screened interaction given by Eq. (11) with the approximation $\chi(q)=1$ (model 4), we also consider a partial treatment of the nonlocality. Following the approximation detailed in Appendix B [see Eq. (B3)], one obtains (model 5)

$$\chi(q)=\frac{1-2I_1(|q|R)K_1(|q|R)}{1-(|q|R)K_1(|q|R)}. \tag{22}$$

In the limit of very narrow wires, $R\to 0$, nonlocal effects vanish. Since $I_1(|q|R)\sim(|q|R)$, it holds $\chi(q)=1$. For increasing values of $|q|R\to\infty$, one finds $\chi(q)\to 0$. Thus, nonlocality tends to suppress the screening action.

4. Models 6 and 7: Density distribution with maximum in wire center

We now consider a strongly inhomogeneous distribution over the wire cross section ($z_0>0$),

$$f(\rho)=\frac{1}{2\pi}\frac{z_0}{\left[\rho^2+z_0^2\right]^{3/2}}, \tag{23}$$

with $N_f=1$. Physically, it characterizes an induced charge density with stronger contributions in the center of the wire cross section. It may be a consequence of the wave function contributing to the polarization response, which decay toward the surface and consequently the vacuum region. Thus, the decaying response exceeds the geometrical wire surface, thereby reflecting some tails of the underlying wave functions and their quantum-mechanical character.

The distribution (23) reaches its maximum at the wire center ($\rho=0$) and decays as $\sim 1/\rho^3$ outside the wire. The parameter z_0 characterizes the lateral extent of the electronic states in the wire. It may be chosen slightly smaller than the geometrical wire radius R; for instance, using $z_0=2R/\sqrt{5}$ ensures that approximately 66% of the electronic response lies within the nominal wire boundary. The corresponding bare potential in Fourier space is derived in Appendix A and reads

$$\widetilde{V}_{\text{bare}}(q)=-2[\cos(|q|z_0)\,\text{ci}(|q|z_0)+\sin(|q|z_0)\,\text{si}(|q|z_0)], \tag{24}$$

where the cosine and sine integral functions $\text{ci}(x)$ and $\text{si}(x)$ have been used (see [57], p. 895, 8.231.1 + 2).

Neglecting nonlocal effects in the screening reaction leads to (local) model 6. A partial inclusion of nonlocality yields [see Appendix B, Eq. (B4)]

$$\chi(q)=\widetilde{V}_{\text{bare}}(2q)/\widetilde{V}_{\text{bare}}(q), \tag{25}$$

which defines (nonlocal) model 7. Because the cosine integral exhibits a logarithmic singularity for vanishing argument, it follows that $\chi(q)=1$ in the limits $z_0\to 0$ or $q\to 0$. For large arguments, the behavior of $\chi(q)$ oscillates around zero as $2\cos(|q|z_0)$.

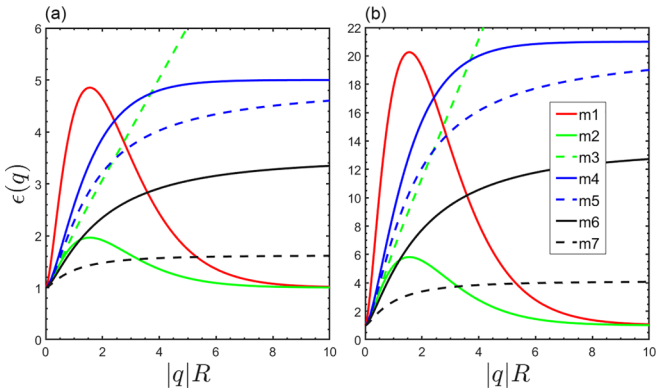


FIG. 2. Effective dielectric function (27) of 1D systems with cross-sectional extent R (with $R = \sqrt{L^2 + h^2}/2$ in the ribbon case) for (a) $\alpha_{1D}/R^2 = 1$ and (b) $\alpha_{1D}/R^2 = 5$. Results for the seven models illustrated in Table I are shown: model 1 (red solid line), model 2 (green solid line), model 3 (green dashed line), model 4 (blue solid line), model 5 (blue dashed line), model 6 (black solid line), and model 7 (black dashed line). The differences between solid and dashed curves illustrate the impact of nonlocality in the screening response.

C. Summary

1. Screening function

The screened potential in Eq. (11) can be rewritten as

$$\widetilde{V}(q) = \frac{\widetilde{V}_{\text{bare}}(q)}{\epsilon(q)}, \tag{26}$$

where the bare Coulomb interaction is reduced by an effective 1D dielectric function

$$\epsilon(q) = 1 + \alpha_{1D} q^2 \chi(q) \widetilde{V}_{\text{bare}}(q). \tag{27}$$

Using the three forms of the bare potential—Eqs. (18) [or, equivalently, Eq. (16)], (21), and (24)—together with the three corresponding treatments of the form factor $\chi(q)$, namely, (i) $\chi(q) = N_f$ neglecting nonlocal effects, (ii) the nonlocal expressions (19) and (22), and (iii) the partially nonlocal form (25), we obtain seven distinct versions of the screening function in Eq. (27), as presented in Fig. 2.

The electronic polarizability term $\sim\alpha_{1D} I_0(|q|R) K_0(|q|R)$ obtained within (nonlocal) model 3 (see Table I) is consistent with expressions previously derived for the screening function of carbon nanotubes [62,63], at least with respect to its prefactor. We note that Eq. (26) may be generalized to include a dielectric environment characterized by a dielectric constant ϵ_0. In the limit of extremely thin wires or nanoribbons, the effective charge e of a carrier must be replaced by the reduced quantity $e/\sqrt{\epsilon_0}$, as discussed in Refs. [4,23,64]. For a nanowire placed at the interface between a dielectric substrate and vacuum, the appropriate effective dielectric constant is given by the average $(\epsilon_0 + 1)/2$, analogous to the standard treatment used for 2D systems [49,50].

For the seven models in Table I, the effective dielectric function $\epsilon(q)$ (27) in Fig. 2 displays the characteristic behavior of a quasi-1D system in the limit of vanishing wave vector, $q \to 0$, i.e., at large real-space separations. In a 1D semiconducting system, the effective electronic polarization vanishes for $q \to 0$, leading to $\lim_{q\to 0} \epsilon(q) = 1$, as previously discussed for nanotubes [23,65]. Thus, in contrast to the 3D semiconductor case, where $\epsilon(0) > 1$, the dielectric constant (to the extent that it can be defined in 1D) remains equal to its vacuum value, $\epsilon(0) = 1$. No net charge is induced by a localized perturbation; indeed, the induced charge given by Eq. (2) integrates to zero [62]. In the opposite limit, $|q| \to \infty$, the seven models in Table I yield different behaviors of $\epsilon(q)$ (27). For the first bare potential $\widetilde{V}_{\text{bare}}(q)$ in Eqs. (16) and (18), whose real-space counterpart is $V_{\text{bare}}(z) = \frac{1}{\sqrt{z^2+R^2}}$ (see Appendix A), and when nonlocal effects are neglected (models 1 and 2), the effective electronic polarization again vanishes for $q \to \infty$. In these cases, for short-distance real-space separations, there is no screening, consistent with predictions for semiconducting nanotubes [23]. When nonlocality is included (model 3), the opposite behavior is found, as displayed in Fig. 2. One finds $\lim_{|q|\to\infty} \epsilon(q) \to\sim q$, a linear trend that is still weaker than the typical q^4 behavior in the 3D case [39], but in agreement with the 2D case, more precisely with the linear screening in the dielectric function appearing in the Fourier-transformed Rytova-Keldysh potential [49,50,55]. However, the second derivative of $\epsilon(q)$ changes signs near $q = 2.3/R$, indicating a nonmonotonic dependence on the wave vector. In the limit of short distances, the Coulomb interaction becomes increasingly screened. This tendency is less pronounced in models 4-7. Their asymptotic behavior $\lim_{q\to\infty} \epsilon(q) = 1 + \alpha_{1D} Q/R^2$ delivers a constant, with $Q = 4$ (models 4 and 5), $Q = 2$ (model 6), and $Q = 0.5$ (model 7). However, the increase is much weaker than in 3D or 2D systems and, importantly, the dielectric function remains finite.

TABLE I. Summary of $\widetilde{V}_{\text{bare}}(q)$ and $\chi(q)$ for different models.

Model	$\widetilde{V}_{\text{bare}}(q)$	$\chi(q)$	Type
1	$2K_0(\lvert q\rvert\sqrt{L^2+h^2}/2)$	4	Local
2	$2K_0(\lvert q\rvert R)$	1	Local
3	$2K_0(\lvert q\rvert R)$	$I_0(\lvert q\rvert R)$	Nonlocal
4	$\frac{4}{q^2R^2}[1 - \lvert q\rvert RK_1(\lvert q\rvert R)]$	1	Local
5	$\frac{4}{q^2R^2}[1 - \lvert q\rvert RK_1(\lvert q\rvert R)]$	$\frac{1 - 2I_1(\lvert q\rvert R)K_1(\lvert q\rvert R)}{1 - \lvert q\rvert RK_1(\lvert q\rvert R)}$	Nonlocal
6	$-2[\cos(\lvert q\rvert z_0)\,\text{ci}(\lvert q\rvert z_0) + \sin(\lvert q\rvert z_0)\,\text{si}(\lvert q\rvert z_0)]$	1	Local
7	$-2[\cos(\lvert q\rvert z_0)\,\text{ci}(\lvert q\rvert z_0) + \sin(\lvert q\rvert z_0)\,\text{si}(\lvert q\rvert z_0)]$	$\widetilde{V}_{\text{bare}}(2q)/\widetilde{V}_{\text{bare}}(q)$	Nonlocal

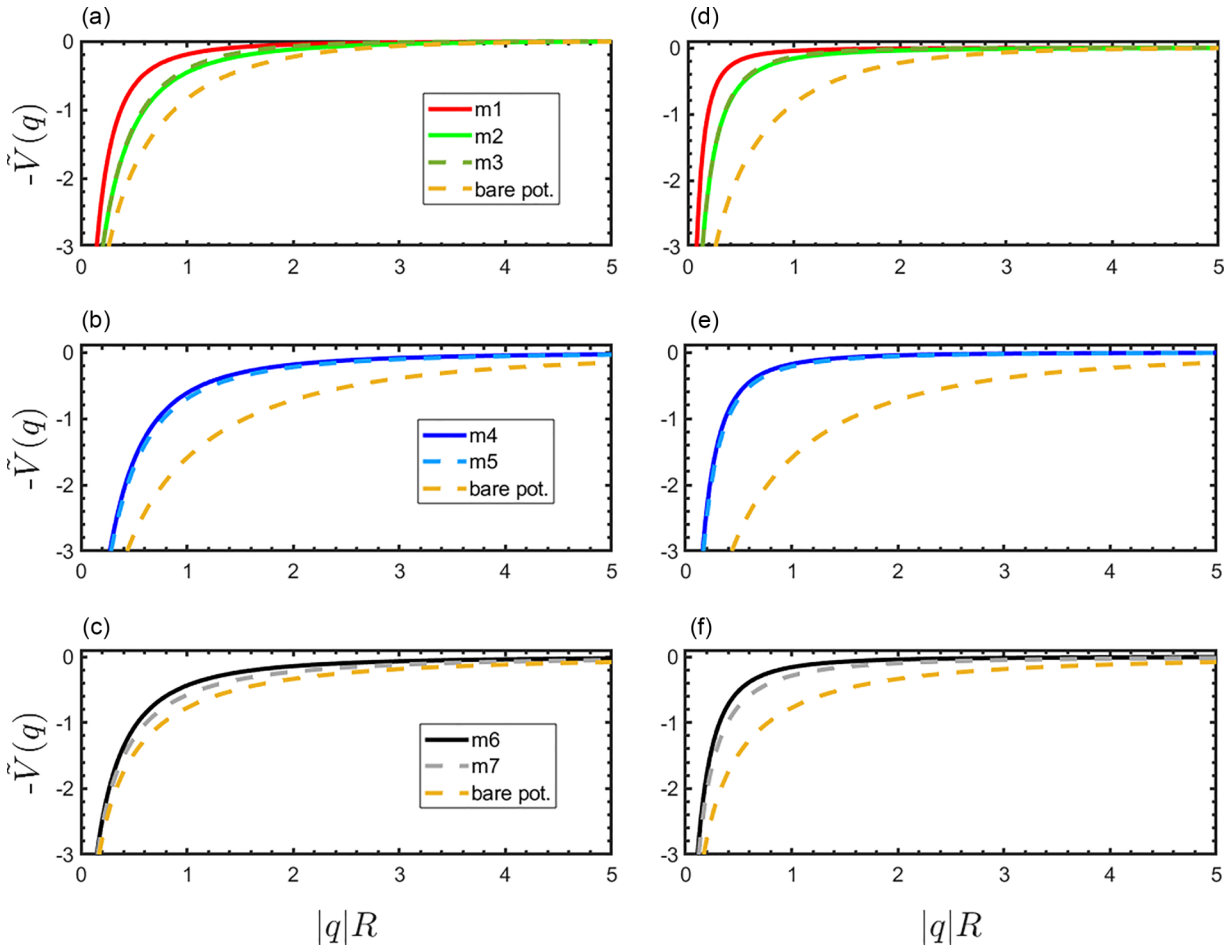


FIG. 3. Screened potential $-\widetilde{V}(q)$ in Fourier space evaluated for the seven models considered in this work. The wave vector $|q|$ is scaled by the characteristic lateral extent $R = \sqrt{L^2 + h^2}/2$ for nanoribbons or by the radius R for a cylindrical wire. Two values of the 1D screening parameter are shown: $\alpha_{1D}/R^2 = 1$ in (a)–(c) and $\alpha_{1D}/R^2 = 5$ in (d)–(f). The results for models 1–7 are displayed as follows: model 1 (red), model 2 (green), model 3 (green dashed), model 4 (blue), model 5 (blue dashed), model 6 (black), and model 7 (gray dashed). For comparison, the corresponding bare (unscreened) Coulomb potentials $-\widetilde{V}_{\text{bare}}(q)$ are shown (yellow dashed). For models 6 and 7, the parameter $z_0 = R$ is used. The three panels on the left and the three on the right correspond to the three different bare potentials defined in Eqs. (A1)–(A3), respectively.

Thus, the polarization strength per cross-sectional area, $\sim\alpha_{1D}/R^2$, merely scales the absolute value of $\epsilon(q)$ at large wave vectors. In all cases, for small real-space distances z, a finite screening effect proportional to α_{1D} persists.

2. *Screened potential*

The consequences of the screening function (27) are illustrated in Fig. 3 for the screened Coulomb potential $-\widetilde{V}(q)$ in Fourier space. The comparison with the unscreened potentials $-\widetilde{V}_{\text{bare}}(q)$ (18), (21), and (24) clearly shows a substantial reduction of the attractive interaction due to screening over a broad range of moderate wave vectors qR. Of course, the magnitude depends on the strength of the 1D electronic polarizability α_{1D}.

As expected, the attractive interaction becomes weaker with increasing α_{1D}. The choice of screening model also plays an important role. For moderate wave vectors, the strongest (weakest) screening effect occurs in model 1 (model 7), as suggested by Fig. 2. The screening strength predicted by models 2–6 lies between these two limits over the same wave vector range. The non-monotonic behavior of $\epsilon(q)$ is particularly pronounced for models 1 and 2, and it gives rise to the antiscreening effects discussed below. In contrast to the screening function $\epsilon(q)$, the nonlocality of the screening reaction plays a minor role, since in the limit $|q|R \to \infty$, i.e., where the nonlocality becomes important, already the averaged bare Coulomb potential $-\widetilde{V}_{\text{bare}}(q)$ tends to vanish.

The real-space dependence of the effective attractive potential energy $W(z)$ defined in Eq. (10) is shown in Fig. 4 for the different approximations of the screening listed in Table I together with the corresponding averaged bare Coulomb potentials $V_{\text{bare}}(z)$ given in Eqs. (A5), (A6), or (A7).

For not too large distances $|z|$, Fig. 4 shows the expected behavior: the attractive interaction is reduced by the screening response of the 1D system. The magnitude of this reduction depends on the chosen screening model and on the value of the static electronic polarizability α_{1D}. More intriguing, however, is the behavior of $W(z)$ at large separations. In this regime, the screened potentials fall below the values of the

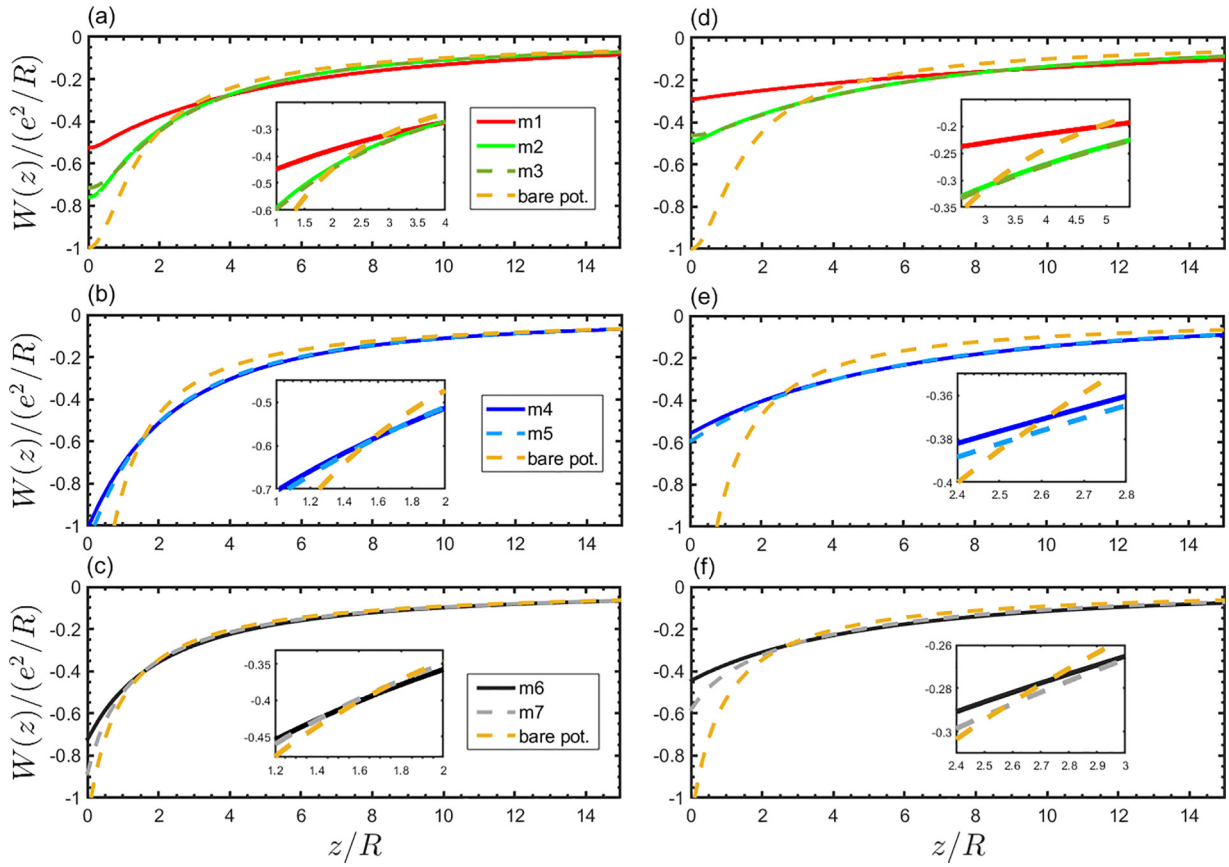


FIG. 4. Screened potential energy $W(z)$ in real space. The electron-hole separation $|z|$ is scaled by the lateral extent R of the 1D object. Two values of the 1D screening parameter are shown: $\alpha_{1D}/R^2 = 1$ (left panels) and $\alpha_{1D}/R^2 = 5$ (right panels). Results for the seven screening models are displayed: model 1 (solid red), model 2 (solid green), model 3 (dashed green), model 4 (solid blue), model 5 (dashed blue), model 6 (solid black) and model 7 (dashed gray). For comparison, the corresponding bare (unscreened) Coulomb potential energies $-e^2V_{\text{bare}}(z)$, expressed in units of e^2/R, are shown as yellow dashed curves for the three bare potentials in Eqs. (A5) (upper panels), (A6) (middle panels), and (A7) (lower panels). The insets highlight the crossings between bare and screened potentials.

corresponding bare interaction $-V_{\text{bare}}(z)$ in the range $z/R = 2-4$, depending on the model and on the screening strength α_{1D}/R^2. This leads to a novel phenomenon, called antiscreening: for electron–hole separations larger than the diameter of the 1D object, the interaction becomes more attractive than the unscreened Coulomb potential. This antiscreening effect originates from the fact that the total induced charge must vanish in a 1D semiconductor, as discussed above.

In this antiscreening region, the induced charge density has the same sign as the external charge density. Such antiscreening behavior has previously been identified in molecular systems [66,67], in carbon nanotubes [23,62] and also in carbon nanoribbons [25].

III. EXCITON PROBLEM

A. Wannier-Mott exciton in 1D

The two-particle electron-hole interaction can in general be formulated as a matrix equation whose Hamiltonian is expressed in terms of the single-quasiparticle Bloch functions [39]. Here, we significantly simplify the many-body treatment in order to describe the lowest-energy bound exciton state with excitation energy $E_1 < E_g$, where E_g denotes the fundamental direct quasiparticle gap of the semiconducting system. Within a two-band model consisting of a conduction band $\varepsilon_c(k)$ and a valence band $\varepsilon_v(k)$, we focus on the excitation energy E_1 and the corresponding exciton binding energy $E_B = E_g - E_1$. Expanding the exciton wave function in terms of relative wave vectors yields the Fourier-transformed envelope function $\phi_n(z)$. In 1D real space, this leads to a two-particle Schrödinger equation for the relative motion of electron and hole [39]

$$\left\{\varepsilon_c\left(-i\frac{d}{dz}\right) - \varepsilon_v\left(i\frac{d}{dz}\right) + W(z)\right\}\phi_n(z) = E_n\phi_n(z) \quad (28)$$

with the statically screened Coulomb interaction $W(z)$ in Eq. (10), which accounts for the long-range electron-hole attraction. The repulsive short-range, unscreened electron-hole exchange interaction is neglected, although it is responsible for the singlet-triplet splitting of the exciton [68]. Due to its strong local character, which can be approximated by a Dirac δ-function $\delta(z)$ [23], its influence on the envelope functions $\phi_n(z)$ is negligible—especially for states satisfying $\phi_n(z = 0) = 0$, as discussed below. In fact, the singlet-triplet splitting in 1D systems is small compared to the exciton binding energy E_B [23].

A further simplification arises from the EMA, i.e., from a parabolic expansion of the band energies near the minimum of

the conduction band c and the maximum of the valence band v. This yields

$$\varepsilon_c\left(-i\frac{d}{dz}\right)-\varepsilon_v\left(i\frac{d}{dz}\right)=E_g-\frac{\hbar^2}{2\mu}\frac{d^2}{dz^2}, \tag{29}$$

where μ is the interband reduced mass defined by $\frac{1}{\mu}=\frac{1}{m_c}+\frac{1}{m_v}$, with m_c and m_v denoting the electron and hole effective masses, respectively. With the kinetic energy of the internal motion $-\frac{\hbar^2}{2\mu}\frac{d^2}{dz^2}$, the two-particle Schrödinger equation (28) describes Wannier-Mott excitons in 1D semiconducting systems [39].

B. Solution without screening

In the limit of vanishing electronic polarizability α_{1D}, the potential $W(z)$ reduces to the bare 1D hydrogenlike polynomials (A5)–(A7) as derived in Appendix A:

$$W(z)=\begin{cases}-\dfrac{e^2}{\sqrt{z^2+R^2}}, & \text{(models 1,2,3)}\\ -\dfrac{2e^2}{R^2}[\sqrt{z^2+R^2}-|z|], & \text{(models 4,5)}\\ -\dfrac{e^2}{|z|+z_0}. & \text{(models 6,7).}\end{cases} \tag{30}$$

The three different forms of the 1D hydrogenic Coulomb potentials in (30) are directly related to the actual distribution function $f(\boldsymbol{\rho})$. The surface distribution (17) leads to the uppermost soft-core potential $\sim 1/\sqrt{z^2+R^2}$, while the homogeneous distribution (20) gives another soft-core potential $\sim[\sqrt{z^2+R^2}-|z|]$ in the middle of expression (30). They relate to each other by an integration

$$\int_0^R d\rho\,\rho\,\frac{1}{\sqrt{z^2+\rho^2}}=2[\sqrt{z^2+R^2}-|z|].$$

The strongly inhomogeneous distribution (23) is related to the truncated potential $\sim 1/(|z|+z_0)$ in (30).

We now consider the limit of very small lateral extent of the 1D system, $R\to 0$. Independently of the specific regularization used for finite R, all three expressions converge to the same asymptotic form:

$$W(z)=-\frac{e^2}{|z|}. \tag{31}$$

It must be emphasized that the potential in Eq. (31) is not the solution of the 1D Maxwell equation for a point charge. Instead, we follow common practice in the literature and refer to it as the 1D Coulomb potential. With Eqs. (29) and (31), the Wannier-Mott exciton problem reduces to the Schrödinger equation of the 1D hydrogen atom, yielding the corresponding eigenvalue problem [69–74].

According to Appendix C, the ground state $n=1$ of the Wannier-Mott-like exciton problem (28), together with Eqs. (29) and (31), is given by

$$E_1=E_g-R_{\rm exc},$$
$$\phi_1(z)=\sqrt{\frac{2}{a_{\rm exc}^3}}ze^{-|z|/a_{\rm exc}}, \tag{32}$$

where $R_{\rm exc}=R_H\mu/m$ is the exciton Rydberg (with R_H the hydrogen Rydberg), and $a_{\rm exc}=\hbar^2/(\mu e^2)$ is the corresponding exciton Bohr radius. This solution describes an unscreened 1D exciton ($R\to 0$) with a binding energy $R_{\rm exc}$ and an average electron–hole separation of $3a_{\rm exc}/2$.

C. Variational solution

In contrast to the true 1D bare potential (31), the electron-hole attraction is described by the statically screened Coulomb potential $W(z)$ in Eq. (10). However, the complexity of this potential energy prevents an analytic solution of the exciton problem (28). We therefore adopt a variational approach for the ground-state exciton ($n=1$), allowing the exciton radius to vary. Specifically, we replace $a_{\rm exc}$ in Eqs. (32) by $a_{\rm exc}/\lambda$, where λ is the variational parameter. The normalized trial function then reads

$$\Phi_{\rm trial}(z)=\sqrt{\frac{2\lambda^3}{a_{\rm exc}^3}}ze^{-\lambda|z|/a_{\rm exc}}, \tag{33}$$

where λ incorporates the effects of (i) the chosen bare potential (A5), (A6), or (A7), and (ii) the screening described by Eq. (26). With (33), the average extent of the exciton bound state, the average distance between electron and hole in real space in the z direction becomes

$$r_B(\lambda)=\int_{-\infty}^{+\infty}dz|z|\phi_{\rm trial}^2(z)=\frac{3}{2}a_{\rm exc}/\lambda. \tag{34}$$

The exciton binding energy E_B, defined as the difference between E_g and the lowest pair energy E_1, and obtained from the Schrödinger equation (28) with kinetic term (29), is evaluated variationally as

$$E_B(\lambda)=\int_{-\infty}^{+\infty}dz\phi_{\rm trial}(z)\left\{\frac{\hbar^2}{2\mu}\frac{d^2}{dz^2}-W(z)\right\}\phi_{\rm trial}(z).$$

Using the Fourier representation (10), this becomes

$$E_B(\lambda)=R_{\rm exc}\left\{-\lambda^2+\lambda\frac{4}{\pi}\int_0^\infty dt\,\frac{1-3t^2}{(1+t^2)^3}\widetilde{V}\left(\frac{2\lambda}{a_{\rm exc}}t\right)\right\}. \tag{35}$$

The extremum condition determines the optimal variational parameter $\lambda=\lambda_0$, so $E_B=E_B(\lambda_0)$ and $r_B=r_B(\lambda_0)$. Because of the complexity of $\widetilde{V}(q)$, the integral over t in Eq. (35) must be evaluated numerically.

The resulting binding energies E_B and exciton radii r_B obtained from the variational procedure are shown in Figs. 5 and 6, respectively.

For relatively small exciton extents $a_{\rm exc}$ compared to the wire radius R [e.g., $a_{\rm exc}/R=1$, as in Fig. 5(a)], i.e., for characteristic average electron-hole separations that are smaller than or comparable to the wire width, one observes—except for very small electronic polarizabilities—the expected trend: the exciton binding energy E_B decreases with increasing 1D electronic polarizability α_{1D} (normalized to R^2). Therefore, the detailed functional dependence varies among the seven models. Nonlocality in the screening response plays only a minor role; except for model 7, it slightly enhances the exciton binding energy. The binding strength depends strongly on the choice of the lateral distribution function $f(\rho)$ Eqs. (15), (17),

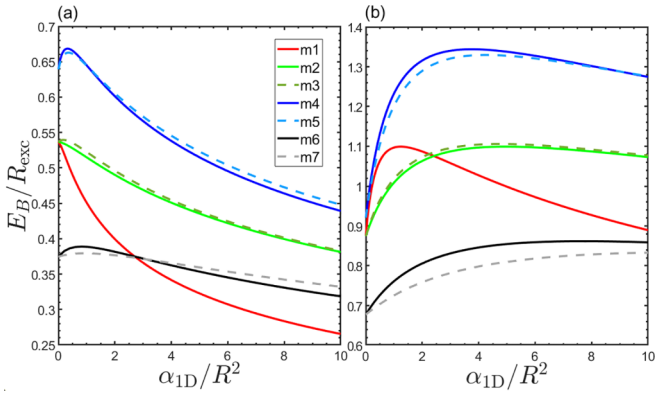


FIG. 5. Exciton binding energy E_B obtained from the variational approach as a function of the screening parameter α_{1D}/R^2. Two characteristic ratios of the exciton radius to the lateral extent, (a) $a_{exc}/R = 1$ and (b) $a_{exc}/R = 5$, are considered. Results for the seven screening models in Table I are shown for different screening reactions: model 1 (solid red), model 2 (solid green), model 3 (dashed green), model 4 (solid blue), model 5 (dashed blue), model 6 (solid black), and model 7 (dashed gray).

(20), or (23)]—that is, on the degree of softening or truncation applied to the bare 1D Coulomb potentials in Eqs. (A5)–(A7). For $\alpha_{1D} = 0$ and $a_{exc}/R = 1$, the binding energies follow a clear ordering: $E_B/R_{exc} = 0.64$ (models 4 and 5), $= 0.54$ (models 1–3), and $= 0.37$ (models 6 and 7). This ordering directly reflects the underlying strength of the respective bare 1D potentials, $-e^2/\sqrt{z^2+R^2}$, $-e^2\frac{2}{R^2}[\sqrt{z^2+R^2}-|z|]$ and $-e^2/[|z|+R]$, respectively, which are dominated by their Fourier transformations $\tilde{V}(q) \approx \tilde{V}_{bare}(q)$ in the limit of vanishing electronic polarization. The crossing of the (local) model 1 binding energy with those of models 6 (local) and 7 (nonlocal) near $\alpha_{1D} \approx 2.7R^2$ is a direct consequence of the stronger polarization influence associated with the larger form factor $\chi(q) = 4$ in Table I.

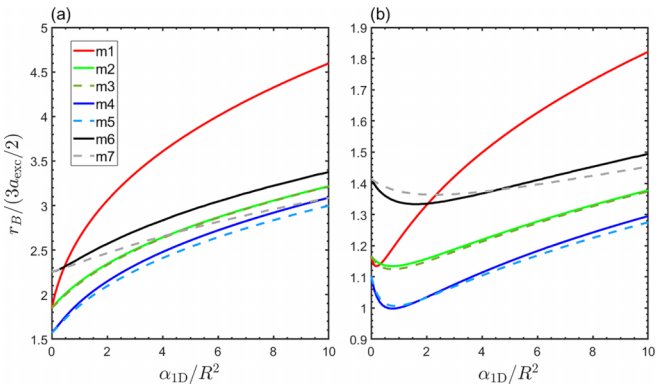


FIG. 6. Average electron–hole separation r_B along the z direction, obtained from the variational procedure, as a function of the screening parameter α_{1D}/R^2. Two characteristic length parameters are considered: (a) $a_{exc}/R = 1$ and (b) $a_{exc}/R = 5$. Results for the seven screening models listed in Table I are shown: model 1 (solid red), model 2 (solid green), model 3 (dashed green), model 4 (solid blue), model 5 (dashed blue), model 6 (solid black), and model 7 (dashed gray).

The drastic increase of a_{exc} relative to the wire radius in the case $a_{exc}/R = 5$ is illustrated in Fig. 5(b). The energetic ordering of the binding energies across the different screening models remains the same as discussed in Fig. 5(a). However, the magnitude of the binding energies is strongly modified. For $\alpha_{1D} = 0$, the binding energies become nearly model-independent, approaching $E_B/R_{exc} \approx 0.9$ (models 1–5) or ≈ 0.7 (models 6 and 7). For finite α_{1D}, a pronounced increase of the binding energy is observed. Near the maxima around $\alpha_{1D}/R^2 \approx 3$, the values of E_B/R_{exc} are roughly twice those obtained for the case $a_{exc}/R = 1$. More precisely, for a broad range of α_{1D}/R^2 values, from zero up to large values determined by the ratio a_{exc}/R, we find binding energies for the screened 1D hydrogen potential that are greater than those obtained in the limit of vanishing electronic polarization. This unusual behavior seems to be a consequence of the antiscreening effect discussed in Fig. 4. There we showed that $W(z) > -e^2V_{bare}(z)$ holds in 1D at sufficiently large distances from the origin $z = 0$. Thus, for systems where the characteristic electron-hole separation $\sim a_{exc}$ [Eq. (34)] greatly exceeds the wire radius R, i.e., for extremely thin wires in terms of excitonic units, the antiscreening contribution becomes dominant, giving rise to the remarkably large binding energies observed. For large electronic polarizabilities, $\alpha_{1D}/R^2 \gg 1$, the antiscreening effect diminishes. The behavior of E_B/R_{exc} then reverts to the normal' monotonic decrease with increasing α_{1D}/R^2, consistent with the trends shown in Fig. 5(a).

Several of the features observed in Fig. 5 have direct implications for the actual average electron–hole distances r_B, which are presented in Fig. 6.

The general trend with increasing electronic polarizability is consistent with expectations: the average electron–hole separation r_B/r_B^0 increases, where $r_B^0 = 3a_{exc}/2$ denotes the radius of the ground-state wave function of the 1D hydrogen atom with potential $-e^2/|z|$. The overall ordering of the curves follows naturally from the corresponding binding energies: larger values of r_B occur in model 1, model 6 (7), model 2 (3), and model 4 (5). For vanishing electronic polarizability, $\alpha_{1D}/R^2 \to 0$, Figs. 6(a) and 6(b) clearly display different limiting behaviors. While r_B/r_B^0 approaches values of 1.1–1.4 for $a_{exc}/R = 5$, it lies in the range 1.6-2.3 for $a_{exc}/R = 1$, in agreement with the expected trends based on the 1D exciton binding. Particularly noteworthy is the visibility of the antiscreening effect in the behavior of r_B. For large values of a_{exc}/R, i.e., for thin wires, the curves in Fig. 6(b) exhibit clear minima at small electronic polarizabilities α_{1D}. We therefore conclude that antiscreening becomes apparent for exciton binding for relatively small effective electronic polarizabilities α_{1D}/R^2 and for wire extents $a_{exc}/R > 1$.

One may also adopt the variational approach used in the 2D case [52] and employ a 1s-like trial function:

$$\Phi_{trial}(z) = \sqrt{\frac{\lambda}{a_{exc}}} e^{-\lambda|z|/a_{exc}}.$$

Interestingly, this choice yields the same kinetic-energy contribution as in Eq. (35). However, the potential-energy term is modified: the factor $(1-3t^2)/(1+t^2)^3$ is replaced by $1/(1+t^2)$. As a consequence, the resulting binding energies are larger. This observation highlights an important difference

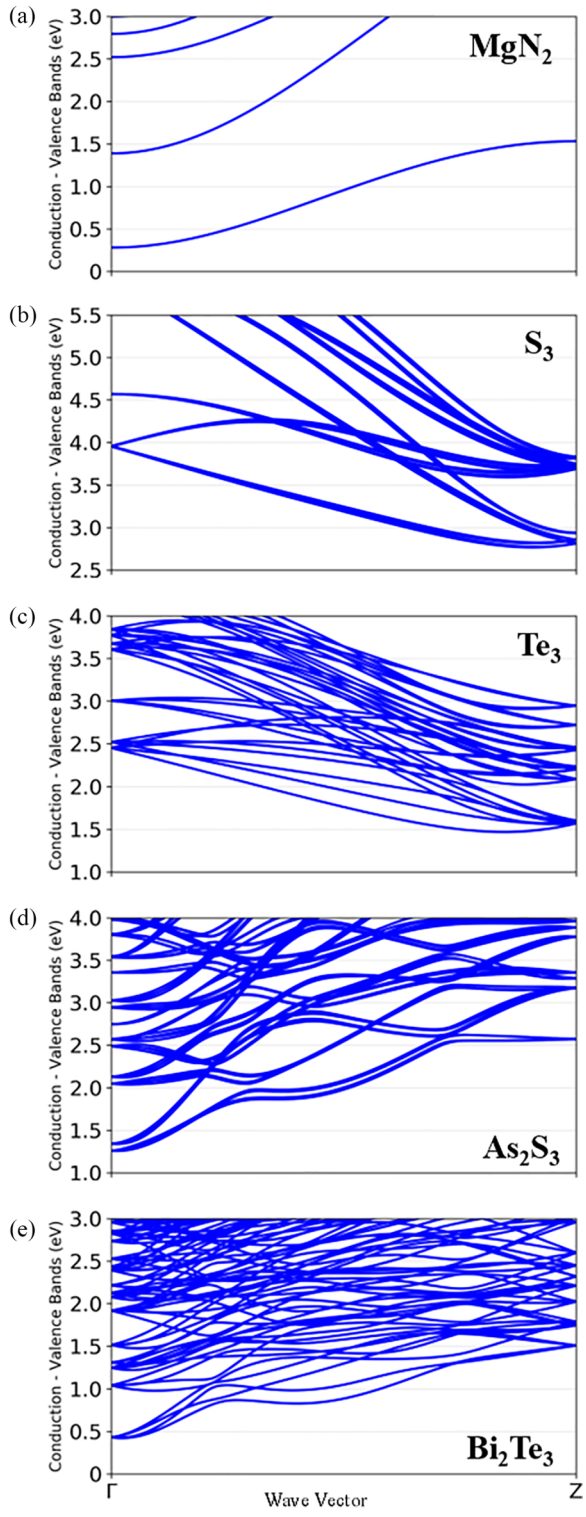


FIG. 7. Kohn-Sham interband structures of quasi-1D systems (a) MgN_2, (b) S_3, (c) Te_3, (d) As_2S_3, and (e) Bi_2Te_3, calculated as differences of conduction and valence bands.

between 1D and 2D excitons. In 1D, the probability of finding the electron and hole at the same position $z = 0$ must vanish, as enforced by both the ground-state wave function ($n = 1$) of the 1D hydrogen atom [Eqs. (32)] and the trial function in Eq. (33).

TABLE II. Parameters of 1D materials considered in this work: geometry parameters L, h, and R (in Å), interband mass μ (in units of the free-electron mass m) and static electronic polarizability α_{1D} (in Å^2).

Material	L	h	R	μ	α_{1D}
MgN_2	2.01	0.74	1.07	0.69	2.18
S_3	3.33	3.12	2.28	0.39	12.06
Te_3	3.12	2.91	2.13	0.30	17.43
As_2S_3	1.91	3.92	2.18	0.16	26.05
Bi_2Te_3	6.24	5.08	4.02	0.11	51.63

IV. SELECTED ATOMIC CHAINS

A. Density functional treatment

To investigate excitonic properties in 1D systems in detail, we consider several atomic chains oriented along z-direction. The systems under study are strongly bonded and energetically stable chains composed of MgN_2, S_3, Te_3, As_2S_3, and Bi_2Te_3 units. Their structural and electronic properties were obtained in Ref. [33] using DFT [41,42] with the Perdew-Burke-Ernzerhof XC functional [75], as implemented in the QUANTUM ESPRESSO package [43,44]. The calculations employed a periodic 3D superlattice geometry with sufficiently large vacuum separations in the x and y directions to ensure isolation of the chains.

In the many-body *GW* and BSE calculations, performed using the YAMBO code [40], a cutoff function for the Coulomb interaction is applied to accelerate convergence. The screened Coulomb potential is computed fully *ab initio*. In Ref. [33], the relaxed atomic geometries are reported, previously selected from a large data set of exfoliable 1D materials [76]. The resulting KS band structures along the 1D Brillouin zone in the $\Gamma - Z$ direction are displayed in Fig. 7. In particular, the interband structures are shown to illustrate the (quasi)continuum of electron-hole pair excitation energies with quasiparticle and excitonic effects.

The treatment of screening within the electrostatic description based on the Poisson equation (1) requires representing the atomic chains or ribbons as defined geometrical objects. Consequently, we mapped the electron charge density onto rectangular or cylindrical geometries. In our fit procedure, we made use only of the geometrical thickness and cross-sectional dimensions. Since the systems can be treated either as nanoribbons or as nanowires, Table II lists both the width L and height h for a rectangular cross section, as well as the corresponding effective radius R for an approximately circular cross section.

Only the energy differences between the lowest unoccupied conduction band and the highest occupied valence band around the fundamental gap—those transitions that predominantly contribute to the lowest-energy electron-hole excitations near the absorption edge—are shown in Fig. 7. MgN_2 is a direct 1D semiconductor, with its fundamental electronic gap located at Γ. The elemental chains S_3 and Te_3 are indirect 1D semiconductors: their interband minima lie along the $\Gamma - Z$ direction near the zone-edge Z, with a second extremum located exactly at Z. However, these two minima differ by less than 0.1 eV. As a result, the lowest excitonic

states in S_3 and Te_3 are expected to originate predominantly from interband transitions in the vicinity of Z. Likewise, As_2S_3 and Bi_2Te_3 exhibit indirect band gaps at approximately 0.3 ΓZ, although a secondary interband minimum appears at Γ with slightly higher energy. As a result, the lowest excitonic states are expected to originate predominantly from interband transitions in the vicinity of Γ.

Within spin and spin-orbit interaction, the interband structures of the chalcogenide chains in Fig. 7 exhibit rather complex band manifolds, even in the vicinity of the lowest allowed interband transitions, with several degeneracies at Γ or Z. In the S_3 and Te_3 cases, near Z, the presence of four nearly degenerate valence bands together with two nearly degenerate conduction bands results in eight possible interband transitions that may contribute to the formation of the lowest exciton bound state. For As_2S_3 and Bi_2Te_3, near Γ, two almost degenerate valence bands and two degenerate conduction bands give rise to four contributing interband pairs. To capture the dominant contributions to the lowest excitonic state within the effective-mass approximation, we perform a parabolic fit of the interband dispersion obtained from the lowest conduction and highest valence bands around the minimum along the $\Gamma - Z$ line. The resulting effective interband masses μ are reported in Table II.

B. Electronic polarizability

The response of the screening electron gas in the 1D object is characterized in Eq. (2) by the static electronic polarizability α_{1D}. Its computation follows strategy used for evaluating the 2D polarizability α_{2D} [77]. Each nanoribbon or nanowire—characterized by the lattice constant $a = 3.823$ (MgN_2), 4.414 (S_3), 5.697 (Te_3), 3.540 (As_2S_3), and 4.342 Å (Bi_2Te_3)—is periodically repeated in the transverse x and y directions using vacuum separations L_x and L_y. These define a 2D rectangular superlattice (SL) in the xy plane. The dielectric and optical properties of the full SL arrangement are computed *ab initio*, for example within DFT, yielding the frequency-dependent dielectric tensor $\hat{\epsilon}^{SL}(\omega)$ in the random-phase approximation (RPA) [39,68] or, more precisely within the independent-particle approximation [39,78]. For low-dimensional systems, it is more convenient to analyze the optical conductivity tensor $\hat{\sigma}^{SL}(\omega)$ rather than $\hat{\epsilon}^{SL}(\omega)$; in cgs units, the two quantities are related by

$$\hat{\epsilon}^{SL}(\omega) = 1 + \frac{4\pi i}{\omega}\hat{\sigma}^{SL}(\omega). \tag{36}$$

To describe the polarization within the isolated 1D object, we focus on the zz component of the dielectric and conductivity tensors, which determines the 1D conductivity along the chain. It is defined as

$$\sigma_{1D}(\omega) = L_x L_y \sigma_{zz}^{SL}(\omega) = \frac{\omega}{4\pi i} L_x L_y \left[\epsilon_{zz}^{SL}(\omega) - 1\right]. \tag{37}$$

In analogy with the Ohm law, this relation connects the electric field appearing in Eq. (2), averaged over the cross section of the 1D object in the xy plane, to the averaged induced 1D current density along the z direction—and, through charge conservation, to the time derivative of the induced charge density. Consequently, the real part of Eq. (37) yields the 1D electronic polarizability, in analogy with the procedure used for 2D materials [79]

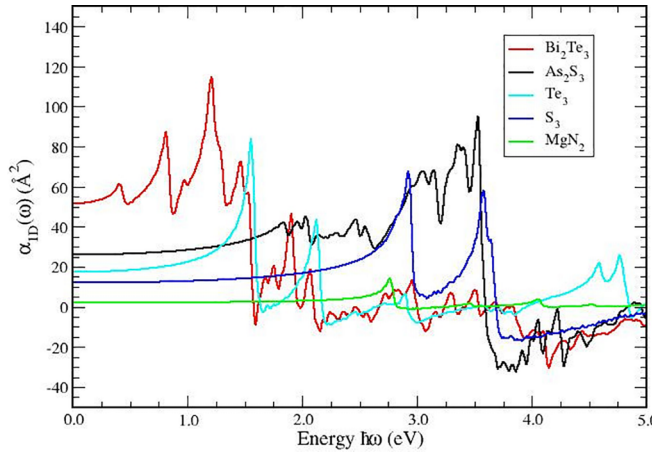


FIG. 8. Real part of the frequency-dependent electronic polarizability α_{1D} for the five atomic wires investigated in this work: MgN_2 (green), S_3 (blue), Te_3 (magenta), As_2S_3 (black), and Bi_2Te_3 (red).

$$\begin{aligned}\alpha_{1D}(\omega) &= -\frac{1}{\omega} Im[\sigma_{1D}(\omega)] \\ &= \frac{1}{4\pi} L_x L_y \left[Re\epsilon_{zz}^{SL}(\omega) - 1\right]\end{aligned} \tag{38}$$

from which the static electronic polarizability follows as $\alpha_{1D} = \alpha_{1D}(0)$.

The resulting frequency-dependent electronic polarizability (38) for the five atomic wires investigated here is shown in Fig. 8.

As expected from their electronic structures shown in Fig. 7, several spectral features emerge in the higher-energy region. The zeros of the real part of the polarizability correspond closely to van Hove singularities in the interband transitions at the associated excitation energies. Interestingly, the spectra of elemental Te_3 and of the compound Bi_2Te_3 exhibit strong similarities above 1.5 eV, reflecting the predominant contribution of Te-derived electronic states in that energy range. For the sulfur-based systems, a comparable correspondence between the S_3 and As_2S_3 spectra appears at energies above 3.5 eV, again indicating the increasing influence of the chalcogen-derived bands at higher excitation energies.

However, the static electronic polarizabilities $\alpha_{1D}(\omega)$ in the limit $\omega \to 0$ differ strongly among the five 1D systems considered. The resulting values α_{1D}, listed in Table II, span a wide range—from about $\alpha_{1D} = 2$ Å^2 for MgN_2 up to nearly 50 Å^2 for Bi_2Te_3. Along the series S_3, Te_3, As_2S_3, Bi_2Te_3, the trend correlates qualitatively with the inverse of the direct Kohn-Sham gap, whose values are 2.76, 1.47, 1.26, and 0.43 eV, respectively. This correlation follows the expected scaling with a prefactor of approximately 24 eV · Å^2 $\approx \pi e^2 a_B$, analogous to the situation encountered in 2D materials [79]. MgN_2 represents an interesting exception: Because the lowest optical transitions are dark, the optical gap (≈2.8 eV) is much larger than the direct electronic gap (0.26 eV). In addition, the material's absorption is very low compared to the other studied compounds, eventually resulting in a substantially reduced polarizability.

TABLE III. Exciton binding energies E_B (in eV) and exciton radii r_B (in Å) for the five 1D materials considered. For each system, results obtained from the seven screening models (1–7) described in the text are reported. For comparison, *ab initio* exciton parameters from Ref. [33] are also included. These *ab initio* values differ depending on the screening used in the Bethe–Salpeter calculations: RPA-like screening constructed from Kohn–Sham eigenvalues and (in parentheses) screening based on quasiparticle energies obtained from a self-consistent *GW* calculation.

	E_B							r_B								
Material	1	2	3	4	5	6	7	1	2	3	4	5	6	7	E_B^{BSE}	r_B^{BSE}
MgN_2	2.95	3.72	3.77	4.56	4.61	2.91	2.91	4.2	3.2	3.2	2.9	2.8	3.5	3.3	1.63 (1.89)	11.5 (11.5)
S_3	1.38	1.80	1.82	2.19	2.22	1.43	1.45	8.7	6.4	6.4	6.0	5.8	6.9	6.5	1.93 (2.27)	12.5 (12.4)
Te_3	1.21	1.62	1.64	1.94	1.97	1.31	1.33	10.6	7.7	7.7	7.2	7.0	8.2	7.7	1.65 (2.14)	14.8 (14.7)
As_2S_3	0.95	1.24	1.25	1.47	1.49	1.00	1.00	15.2	11.2	11.1	10.5	10.3	12.0	11.3	0.89 (0.33)	12.0 (14.4)
Bi_2Te_3	0.62	0.78	0.79	0.94	0.95	0.62	0.61	22.2	16.7	16.6	15.5	15.1	18.1	17.2	0.77 (0.85)	13.2 (13.2)

The *ab initio* calculations for other infinitely long quasi-1D systems, such as oligomers, yield static electronic polarizabilities α_{1D} on the order of $10\pi R^2$, when expressed in terms of the cross-sectional area [60]. For radii of about 1–3 Å, this corresponds to absolute values of $\alpha_{1D} \approx 30$–100 Å^2. These values are of the same order of magnitude as the polarizabilities of the chalcogenides listed in Table II.

C. Solution of the BSE

The *ab initio* calculation of the exciton binding energy of the lowest electron–hole excitation below the fundamental absorption edge requires, as a first step, the determination of the quasiparticle electronic structure, typically within Hedin's *GW* framework for the XC self-energy [39]. We distinguish between the single-shot G_0W_0 and the self-consistent *GW* approach, in which both the single-particle Green's function G and the screened Coulomb interaction W (more precisely, the dielectric matrix entering W) are iteratively updated until convergence is achieved. In this way, the direct Kohn–Sham gaps are widened to the quasiparticle (QP) values $E_g = 4.76/5.59$ (MgN_2), 5.55/6.34 (S_3), 3.50/4.31 (Te_3), 2.30/3.04 (As_2S_3), and 1.54/1.65 (Bi_2Te_3) eV within G_0W_0/GW.

The G_0W_0 and *GW* band structures, together with the KS wave functions, are then used to construct the two-particle Hamiltonian in the Tamm-Dancoff approximation [39]. In this construction, typically up to 12 empty and filled bands are included. The screened interation W_0 and W also enters the attractive electron-hole term of the Hamiltonian. The diagonalization of the Hamiltonian yields the excitation energy E_1 of the lowest (bound) excitonic state. The exciton binding energy is then obtained as $E_B^{\mathrm{BSE}} = E_g - E_1$. Explicitly, these calculations were performed using the YAMBO code [40]. The resulting binding energies E_B^{BSE} for the various materials and screening models are summarized in Table III. The BSE analysis also provides the exciton radius r_B^{BSE}, computed from the expectation value of the electron–hole separation for a fixed hole position.

V. DISCUSSION

A. Exciton binding

Explicit values of E_B and r_B for the seven screening models under consideration have been obtained using the parameters α_{1D} and μ within the variational scheme of Eq. (35) and are reported in Table III.

The resulting exciton parameters, namely, the binding energy E_B and the exciton radius r_B, show a clear sensitivity to the geometry, effective mass, and polarization parameters. In effective units, with the binding energy E_B expressed in excitonic Rydbergs R_{exc}, the wire radius R in excitonic units a_{exc}, and the electronic polarizability α_{1D} normalized by the cross-sectional area R^2, Fig. 5 illustrates the influence of these parameters over a wide range of values. However, for a given screening model, small variations in these parameters lead only to small variations in the resulting exciton binding energy.

The magnitude of the exciton binding energies spans a broad range, $E_B = 0.6 - 4.6$ eV, depending on the specific 1D material and the screening model employed. These values are consistent with the order of magnitude found in other quasi-1D systems, such as 0.7 eV [26], around 1.0 eV [21–23], and $0.5 - 3.0$ eV [25]. Among the chalcogen-based chains S_3, Te_3, As_2S_3, Bi_2Te_3, the binding energies follow a clear chemical trend: larger polarizabilities α_{1D} and smaller interband masses μ correlate with reduced E_B. This trend is further supported by the MgN_2 wire, which combines the smallest α_{1D} with the largest μ. The screening model itself also affects the resulting binding energies. The form factor $\chi(q)$ in Table I, which distinguishes (local) models 2, 4, and 6 from their partially-nonlocal counterparts 3, 5, and 7, slightly modifies the screening behavior (see Figs. 3 and 4), but only weakly influences the final exciton binding energies (Table III). For example, replacing $\chi(q) = 1 \to I_0(|q|R)$ when going from (local) model 2 to (nonlocal) model 3 produces only a minimal change, indicating that the relevant $|q|$-range is restricted and dominated by the long-range part of the electron–hole interaction. Overall, screening plays a crucial role even in 1D systems: it reduces E_B by factors of 2 to 3 relative to the exciton Rydberg R_{exc}. In a simplified picture of Coulomb screening by a homogeneous dielectric, such factors may be identified as an effective dielectric constant. The specific form of the bare potential $\widetilde{V}_{\mathrm{bare}}(q)$ [Eqs. (A1), (A2), or (A3)] used for a finite cross section also plays a role. associated with the finite cross section also impacts the binding energy. A consistent ordering appears across all five 1D materials: model 6, 7 < model 2, 3 < model 4, 5. These trends in binding energies are mirrored by the exciton radii r_B, which vary substantially, from 2.8 to 22.2 Å, depending on the material and

screening model. The radii likewise follow clear chemical trends associated with α_{1D} and μ, and show systematic differences between models 1–7.

B. Model evaluation

For comparison, *ab initio* values of E_B^{BSE} and r_B^{BSE} [33] are also listed in Table III. The *GW* calculations are performed both without self-consistency (G_0W_0), and including self-consistency, which substantially increases the fundamental gaps. Accordingly, the homogeneous BSE is solved using two different screened electron–hole interactions, W_0 and W. This procedure yields two distinct binding energies, both of which show the same order of magnitude as the variational results obtained within the EMA using a static electronic polarizability for the various screening models. Despite some dependence on self-consistency in the BSE and on the chosen α_{1D}, we find excellent agreement between the model and *ab initio* results for the chalcogen-containing chains S_3, Te_3, As_2S_3, and Bi_2Te_3. For MgN_2, however, the *ab initio* binding energies are smaller than the model predictions.

For exciton radii, a similar trend is observed. Independently of the model, the calculated values of r_B are smaller than the corresponding *ab initio* values r_B^{BSE}; see Table III. However, this discrepancy decreases significantly along the series MgN_2, ..., Bi_2Te_3, i.e., with decreasing optical gap. Similar trends have been observed when comparing model and *ab initio* results for 2D materials, for example for 2D group-III nitrides [80,81].

While the chemical trend along MgN_2, S_3, Te_3, As_2S_3, and Bi_2Te_3 is less pronounced in the BSE results, it generally follows the expected trend of decreasing fundamental gap (with the exception of the interchange between MgN_2 and S_3). The discrepancies between the model results and the combined BSE + *GW* treatment arise from several sources: (i) the complexity of the QP band structures (Fig. 7) and the parabolic approximation of the interband dispersion in the EMA, and (ii) the simplified model screening of Table I, which compresses the entire dielectric response into a single parameter α_{1D}. Similar levels of agreement—and discrepancy—are observed for the exciton radii for r_B and r_B^{BSE} in Table III.

From the close or partial agreement between model-derived and *ab initio* exciton binding energies, one may attempt to identify the best' screening model. For MgN_2, models 6 and 7, based on the cutoff bare potential in Eq. (A7), yield the closest values of E_B, although a noticeable overestimation—equivalently, an underestimation of screening—still persists. Much better agreement is found for models 2 and 3 (models 4 and 5) for the elemental chalcogenides S_3 and Te_3 when compared with BSE results using W_0 (W). For As_2S_3 and Bi_2Te_3, the best agreement is obtained with models 6 and 7, and to some extent also with model 1. In fact, for the smallest-gap material Bi_2Te_3, all screening models yield binding energies close to the *ab initio* values.

Importantly, the inclusion of nonlocality in the screening has only a minor effect and may safely be neglected. The binding energies are far more sensitive to the choice of the bare 1D hydrogenic potential, $1/\sqrt{z^2+R^2}$ (models 1, 2, 3), $2[\sqrt{z^2+R^2}-|z|]/R^2$ (models 4, 5) or $1/[|z|+z_0]$ (models 6, 7), and therefore to the assumed spatial extent of the screening charge distribution. This extent—localized at the surface, spread uniformly across the cross-section, or peaked at the wire center—is encoded in the distribution functions $f(\rho)$ of Eqs. (17), (20), and (23), respectively.

VI. SUMMARY

In summary, starting from a continuum description and a characterization of the quasi-1D electron gas by a constant static electronic polarizability α_{1D}, computed from first principles, we have derived analytical expressions for the Fourier transform of the statically screened Coulomb potential. Depending on how the induced charge density is distributed across the cross section of the 1D system and on the treatment of nonlocal screening effects, seven distinct screening models were formulated. Finding a universal model for a screened potential in 1D is much more difficult than in the 2D case of the Rytova-Keldysh potential for at least two reasons. First, there is no analog in 1D of the limit of vanishing sheet thickness because logarithmic singularities appear for vanishing lateral extent R or L of the 1D objects. Moreover, the small-wave-vector limit of the screened potentials is insufficient because important 1D features such as antiscreening cannot be described. Second, the singular true bare 1D hydrogen potential $\sim 1/|z|$ does not appear for vanishing electronic polarization $\alpha_{1D} = 0$. Rather, the transition from the quasi-1D behavior to the true 1D limit requires some assumption about the distribution function $f(\boldsymbol{\rho})$, resulting in different so-called soft-core or truncated 1D hydrogen potentials, which nevertheless reproduce the singularity at $z = 0$ for vanishing R or L. We apply almost three different distributions and therefore use three different bare potentials. Together with whether the nonlocality in screening is neglected or not, this leads to several models for the screened electrostatic potential in 1D, which are discussed here.

To describe the internal relative motion of electron–hole pairs, the interband energy dispersion was approximated within the EMA. Because of the complexity of the screened interaction, a fully analytical solution of the resulting exciton equation is not feasible. Therefore, a variational approach was employed, using as trial function the ground-state wave function of the 1D hydrogen atom. This framework was applied to representative chain-like quasi-1D semiconductors: MgN_2, S_3, Te_3, As_2S_3, and Bi_2Te_3. The resulting exciton binding energies from the variational approach fall in the range of about 1 eV, consistent with values reported for many other quasi-1D systems such as nanoribbons, quantum wires, and hydrogenated carbon chains. Even larger binding energies are predicted for wide-gap materials, particularly MgN_2. Clear chemical trends emerge that correlate the exciton binding energy with the static polarizability and the reduced interband mass.

A comparison with exciton binding energies obtained from first-principles many-body calculations—specifically, *GW* quasiparticle energies combined with solutions of the Bethe-Salpeter equation—confirms the reliability of the model based on the novel 1D screened electrostatic potentials to describe the electron-hole attraction and the EMA to characterize the internal motion of the electron-hole pairs. Comparing *ab initio* and model results for the exciton binding, good agreement is

found both for the absolute magnitudes and for the chemical trends across the material series. For some screening models, especially those based on truncated or soft-core 1D hydrogenic potentials, the agreement with the *ab initio* results is even excellent. The best agreement depends on the 1D chain material, especially on its fundamental gap. For MgN_2, with a quasiparticle gap of about 5 eV, screening models 6 and 7, based on the truncated 1D hydrogen potentials, tend to give binding energies close to the *ab initio* ones. In the case of the elemental chalcogen chains, with quasiparticle gaps near 6.3 or 4.3 eV, almost all models deliver results close to those computed within BSE. For the 1D group-V chalcogenides, with gaps around 3.0 and 1.7 eV, similar conclusions hold. In any case, the screening models give rise to the same trend in binding energies as the BSE solutions. Beyond providing physical insight, these model screening functions offer a computationally inexpensive alternative to full GW + BSE calculations: once the geometry, effective masses, and static 1D polarizability are known, exciton binding energies can be estimated rapidly within the variational framework, making the approach suitable for comparing screening models and for surveying larger sets of quasi-1D materials.

ACKNOWLEDGMENTS

We acknowledge CINECA's, for the availability of high-performance computing resources and support. F.B. and O.P. are grateful to INFN for support through the TIME2QUEST project. We thank G. Bärwolff (TU Berlin) for help in constructing the distribution function (23).

DATA AVAILABILITY

There are no publicly available research data or software supporting this manuscript. Requests for further information or data should be sent to the authors.

APPENDIX A: BARE COULOMB POTENTIAL IN CYLINDRICAL QUANTUM WIRES

For the Coulomb interaction along the wire direction but localized near the surface of the system with vanishing cross section, we obtain Eq. (18):

$$\widetilde{V}_{\text{bare}}(q) = 2K_0(|q|R). \tag{A1}$$

If instead the interaction is homogeneously smeared over the entire wire cross section using the distribution function $f(\rho)$ in Eq. (20), one finds

$$\widetilde{V}_{\text{bare}}(q) = 4\int_0^1 dx x K_0(|q|Rx).$$

The integral over the Bessel function can be evaluated analytically. Using Ref. [57], p. 684 (6.561.8), the result becomes

$$\widetilde{V}_{\text{bare}}(q) = \frac{4}{|q|^2R^2}[1 - |q|RK_1(|q|R)]. \tag{A2}$$

For the inhomogeneous distribution $f(\rho)$ of Eq. (23), the averaged bare Coulomb potential in Fourier space [Eq. (12)] reads

$$\widetilde{V}_{\text{bare}}(q) = 2\int_0^\infty dx \frac{x}{(x^2+1)^{3/2}} K_0(|q|z_0x).$$

Using the integral representation $K_0(ax) = \int_0^\infty dy \frac{yJ_0(ay)}{y^2+x^2}$ (see [57], p. 679, 6.532.4) and $\int_0^\infty dx \frac{xJ_0(bx)}{(x^2+1)^{3/2}} = e^{-b}$ (see [57], p. 683, 6.554.4), the result simplifies to

$$\widetilde{V}_{\text{bare}}(q) = 2\int_0^\infty dy \frac{y}{y^2+1} e^{-|q|z_0y}.$$

Evaluating this integral (Ref. [57], p. 344, 3.354.2) yields

$$\widetilde{V}_{\text{bare}}(q) = -2[\cos(|q|z_0)ci(|q|z_0) + \sin(|q|z_0)si(|q|z_0)], \tag{A3}$$

with the integral cosine (sine) $ci(x)$ [$si(x)$], sometimes denoted $ci(x) = Ci(x)$ and $si(x) = Si(x) - \frac{\pi}{2}$ [57].

More interesting are the Fourier-transformed potentials in real space. With (3) or (10) and the mirror symmetry, one obtains

$$V_{\text{bare}}(z) = \frac{1}{\pi}\int_0^\infty dq \cos(qz)\widetilde{V}_{\text{bare}}(q). \tag{A4}$$

In the first case (A1), it holds

$$V_{\text{bare}}(z) = \frac{2}{\pi}\int_0^\infty dq \cos(qz)K_0(qR)$$

or, applying Ref. [57] (p. 739, 6.699.12), the soft-core 1D hydrogen potential [82,83]:

$$V_{\text{bare}}(z) = \frac{1}{\sqrt{z^2+R^2}}. \tag{A5}$$

For the second version of the bare potential (A2), we apply the representation above and find

$$V_{\text{bare}}(z) = \frac{4}{\pi}\int_0^1 dx x \int_0^\infty dq \cos(qz)K_0(qRx).$$

With the Fourier-transformed quantity (A5), this expression simplifies to

$$V_{\text{bare}}(z) = \frac{2}{R}\int_0^1 dx \frac{x}{\sqrt{x^2+(z/R)^2}}$$

or simply to another form of a soft-core 1D hydrogen atom potential:

$$V_{\text{bare}}(z) = \frac{2}{R^2}[\sqrt{z^2+R^2} - |z|]. \tag{A6}$$

In the third version of $\widetilde{V}_{\text{bare}}(q)$ (A3), the Fourier transform (A4) yields

$$\begin{aligned} V_{\text{bare}}(z) = -\frac{1}{\pi}\int_0^\infty dq\{&[\cos(q(z+z_0)) + \cos(q(z-z_0))] \\ &+ \text{ci}(qz_0) + [\sin(q(z+z_0)) \\ &- \sin(q(z-z_0))]\,\text{si}(qz_0)\}. \end{aligned}$$

By applying the integrals listed in Ref. [57] (pp. 649 and 650, 6.252.1-4), and after some rearrangements, while using the symmetry relation $V_{\text{bare}}(z) = V_{\text{bare}}(-z)$, one obtains

$$V_{\text{bare}}(z) = \frac{1}{|z| + z_0}. \tag{A7}$$

This expression represents a cutoff or truncated Coulomb potential for the 1D hydrogen atom [69,74], where the singularity at $z = 0$ is removed and replaced by the finite value $1/z_0$. The cutoff parameter z_0 may be chosen close to the geometric extent R of the cylindrical wire, reflecting the finite lateral spread of the electronic charge.

Remarkably, in the limit of vanishing cross section, $R \to 0$, all three bare Coulomb potentials derived in Eqs. (A5)–(A7) converge to the same 1D Coulomb form [74]:

$$\lim_{R\to 0} V_{\text{bare}}(z) = \frac{1}{|z|}. \tag{A8}$$

APPENDIX B: NONLOCALITY IN SCREENING REACTION

The form factor (13) accounts for the nonlocality of the screening response. In the case of a homogeneously smeared out induced charge density (20), no exact analytical description is possible. Therefore, we approximate the potential $\widetilde{\widetilde{\varphi}}(\boldsymbol{\rho}', q)$ in the denominator of (13) by its lateral average (8). This leads to the simplified form

$$\chi(q) = \frac{\int d^2\boldsymbol{\rho} f(\boldsymbol{\rho}) \int d^2\boldsymbol{\rho}' f(\boldsymbol{\rho}') K_0(|q||\boldsymbol{\rho} - \boldsymbol{\rho}'|)}{\int d^2\boldsymbol{\rho} f(\boldsymbol{\rho}) K_0(|q|\rho)}. \tag{B1}$$

Using the definition of the Bessel functions $K_0(x)$ (6) and $J_0(x) = \frac{1}{2\pi}\int_0^{2\pi} d\varphi e^{ix\cos\varphi}$ (see [57], p. 921, 8.411.1) and inserting the distribution (20), Eq. (B1) becomes

$$\chi(q) = \frac{2}{R^2} \frac{\int_0^\infty dQ \frac{Q}{Q^2+q^2}\left[\int_0^R d\rho \cdot \rho J_0(Q\rho)\right]^2}{\int_0^R d\rho \cdot \rho K_0(|q|\rho)}. \tag{B2}$$

The denominator is identical to the integral leading to Eq. (A2), and therefore given analytically by Eq. (A3). The numerator I can be rewritten using (see [57], p. 680, 6.541.1, and $q > 0$)

$$\int_0^\infty dQ \frac{Q}{Q^2+q^2} J_0(Q\rho) J_0(Q\rho') = \begin{cases} I_0(q\rho')K_0(q\rho), & \text{for } \rho > \rho' \\ I_0(q\rho)K_0(q\rho'), & \text{for } \rho < \rho', \end{cases}$$

which yields

$$\begin{aligned} I &= \int_0^R d\rho\, \rho \left\{ \int_0^\rho d\rho'\, \rho'\, I_0(q\rho')K_0(q\rho) + \int_\rho^R d\rho'\, \rho'\, I_0(q\rho)K_0(q\rho') \right\} \\ &= \frac{1}{q^4}\int_0^{Rq} dx \left\{ xK_0(x)\int_0^x dy\, yI_0(y) + xI_0(x)\int_x^{Rq} dy\, yK_0(y) \right\}. \end{aligned}$$

First derivations can be introduced according to Ref. [57] (p. 937, 8.486.5 and p. 938, 8.486.15)

$$xI_0(x) = \frac{d}{dx}[xI_1(x)],$$
$$-xK_0(x) = \frac{d}{dx}[xK_1(x)].$$

It results in

$$I = \frac{1}{q^4}\int_0^{Rq} dx \left\{ -\frac{d}{dx}[xK_1(x)]\int_0^x dy\, yI_0(y) + \frac{d}{dx}[xI_1(x)]\int_x^{Rq} dy\, yK_0(y) \right\}$$

or, with the application of the product rule of differentiation,

$$I = \frac{1}{q^4}\int_0^{Rq} dx \left\{ -\frac{d}{dx}\left[xK_1(x)\int_0^x dy \cdot yI_0(y)\right] + x^2K_1(x)I_0(x) + \frac{d}{dx}\left[xI_1(x)\int_x^{Rq} dy \cdot yK_0(y)\right] + x^2I_1(x)K_0(x) \right\}.$$

With the functional relationship of Bessel functions (see [57], p. 936, 8.477.2),

$$I_0(x)K_1(x) + I_1(x)K_0(x) = \frac{1}{x},$$

one finds the expression

$$I = \frac{R^2}{2q^2}\left[1 - \frac{2}{Rq}K_1(Rq)\int_0^{Rq} dy \cdot yI_0(y)\right]$$

and, finally,

$$I = \frac{R^2}{2q^2}[1 - 2I_1(Rq)K_1(Rq)].$$

Consequently, the final result of the form factor (B2) is

$$\chi(q) = \frac{1 - 2I_1(|q|R)K_1(|q|R)}{1 - (|q|R)K_1(|q|R)}. \tag{B3}$$

In the limit of narrow wires $R \to 0$, it holds $I_1(|q|R) = \frac{1}{2}(|q|R)$. The nonlocal effects vanish in this limit. The form factor (B3) becomes

$$\chi(q) = 1,$$

consistent with the approximate solutions (14) and (9).

For the distribution function $f(\rho)$ (23) a similar expression, a Hankel transformation, as (B2) in the case of the homogeneous distribution follows for the form factor (13):

$$\chi(q) = \frac{2\int_0^\infty dQ \frac{Q}{Q^2+q^2}\left[\int_0^\infty d\rho \cdot \rho \frac{z_0}{(\rho^2+z_0^2)^{3/2}} J_0(Q\rho)\right]^2}{\widetilde{V}_{\text{bare}}(q)}.$$

The ρ-integral delivers the exponential function e^{-z_0Q} following [57] (p. 683, 6.554.4). It results in

$$\chi(q) = \frac{2\int_0^\infty dQ \frac{Q}{Q^2+q^2} e^{-2z_0Q}}{\widetilde{V}_{\text{bare}}(q)}$$

and (see [57], p. 344, 3.354.2)

$$\chi(q) = \frac{\cos(2z_0|q|)ci(2z_0|q|) + \sin(2z_0|q|)si(2z_0|q|)}{\cos(z_0|q|)ci(z_0|q|) + \sin(z_0|q|)si(z_0|q|)}, \tag{B4}$$

where the integral cosine (sine) functions $ci(x)$ $[si(x)]$ (see [57], p. 895, 8.230.1 + 2) appear. In the limits of $|q| \to 0$ or small cutoff parameters z_0, it also holds:

$$\lim_{q\to 0} \chi(q) = 1.$$

APPENDIX C: 1D HYDROGEN ATOM

In the limit of vanishing lateral extents of the 1D objects, $R \to 0$, the two-particle problem (28), together with Eqs. (29) and (31), reduces to the single-particle Schrödinger equation

$$\left\{E_g - \frac{\hbar^2}{2\mu}\frac{d^2}{dz^2} - \frac{e^2}{|z|}\right\}\phi_n(z) = E_n\phi_n(z), \tag{C1}$$

where μ is the interband reduced mass. To render Eq. (C1) dimensionless, we introduce the excitonic Rydberg $R_{\rm exc} = R_H\mu/m$ and radius $a_{\rm exc} = a_B m/\mu$ in analogy with atomic units, such that $R_{\rm exc} = \hbar^2/(2\mu a_{\rm exc}^2) = e^2/2a_{\rm exc}$ and $a_{\rm exc} = \hbar^2/(\mu e^2)$. With the substitutions $z = a_{\rm exc}x$ and $\phi(a_{\rm exc}x) = \varphi(x)$, Eq. (C1) becomes [69–73]

$$\left\{\frac{d^2}{dx^2} + \frac{2}{|x|} + \varepsilon_n\right\}\varphi_n(x) = 0, \tag{C2}$$

where $\varepsilon_n = (E_n - E_g)/R_{\rm exc}$. General solutions to Eq. (C2) can be expressed in terms of confluent hypergeometric functions [72] or Whittaker functions [71].

For bound states ($\varepsilon_n < 0$, i.e., $E_n < E_g$) the wave function must decay exponentially for $|x| \to \infty$. This requirement yields the quantization condition

$$\varepsilon_n = -\frac{1}{n^2}, \tag{C3}$$

with quantum numbers $n = 1, 2, \ldots$. The corresponding normalized eigenfunctions may be written [57,71] (see Whittaker differential equation in [57], p. 1033, 9.220.1)

$$\varphi_n(x) = C_n x e^{-|x|/n}\,{}_1F_1\left(1-n, 2; \frac{2|x|}{n}\right), \tag{C4}$$

with the confluent hypergeometric function ${}_1F_1$ and the normalization constant $C_n = \sqrt{\frac{2}{n^3}}$ (see orthogonality relation in [57], p. 1012, 8.980). The major problem related to the discontinuity of the ordinary differential equation (C2) has been discussed and solved elsewhere [71]. Because of the integer arguments $n+1$ and 2, the confluent hypergeometric function can be replaced by (associated) Laguerre polynomials ${}_1F_1(1-n, 2; z) = \frac{1}{n}L_{n-1}^1(z) = -\frac{1}{n}L_n'(z)$ with (see [57], p. 1010, 8972.1)

$$L_n(z) = e^z\frac{d^n}{dz^n}(e^{-z}z^n) \tag{C5}$$

and its derivative $L_n'(z)$ (see also [74]).

We focus on the ground state $n = 1$ with $L_1'(2) = -1$ and therefore

$$\varphi_1(x) = \sqrt{2}xe^{-|x|}$$

or

$$\phi_1(z) = \sqrt{\frac{2}{a_{\rm exc}^3}}ze^{-|z|/a_{\rm exc}}. \tag{C6}$$

This wave function fulfills the boundary conditions $\phi_1(0^+) = \phi_1(0^-)$ and $\frac{d}{dz}\phi_1(z)|_{z=0^+} = \frac{d}{dz}\phi_1(z)|_{z=0^-}$.

[1] O. M. Auslaender, A. Yacoby, R. de Picciotto, K. W. Baldwin, L. N. Pfeiffer, and K. W. West, Tunneling spectroscopy of the elementary excitations in a one-dimensional wire, Science **295**, 825 (2002).

[2] D. Gershoni, J. S. Weiner, S. N. G. Chu, G. A. Baraff, J. M. Vandenberg, L. N. Pfeiffer, K. West, R. A. Logan, and T. Tanbun-Ek, Optical transitions in quantum wires with strain-induced lateral confinement, Phys. Rev. Lett. **65**, 1631 (1990).

[3] E. Kapon, D. M. Hwang, and R. Bhat, Stimulated emission in semiconductor quantum wire heterostructures, Phys. Rev. Lett. **63**, 430 (1989).

[4] T. Ogawa and T. Takagahara, Optical absorption and Sommerfeld factors of one-dimensional semiconductors: An exact treatment of excitonic effects, Phys. Rev. B **44**, 8138 (1991).

[5] S. Glutsch, D. S. Chemla, and F. Bechstedt, Fano resonances in the optical spectra of semiconductor quantum structures, Phys. Rev. B **51**, 16885 (1995).

[6] P. C. Snijders and H. H. Weitering, *Colloquium*: Electronic instabilities in self-assembled atom wires, Rev. Mod. Phys. **82**, 307 (2010).

[7] S. Guo, J. Fu, P. Zhang, C. Zhu, H. Yao, M. Xu, B. An, X. Wang, B. Tang, Y. Deng, *et al.*, Direct growth of single-metal-atom chains, Nat. Synth. **1**, 245 (2022).

[8] P. Ferstl, L. Hammer, C. Sobel, M. Gubo, K. Heinz, M. A. Schneider, F. Mittendorfer, and J. Redinger, Self-organized growth, structure, and magnetism of monatomic transition-metal oxide chains, Phys. Rev. Lett. **117**, 046101 (2016).

[9] H. Yan, J. N. Hohman, F. H. Li, C. Jia, D. Solis-Ibarra, B. Wu, J. E. Dahl, R. M. Carlson, B. A. Tkachenko, A. A. Fokin, *et al.*, Hybrid metal–organic chalcogenide nanowires with electrically conductive inorganic core through diamondoid-directed assembly, Nat. Mater. **16**, 349 (2017).

[10] Q. Xiao, J. A. Burg, Y. Zhou, H. Yan, C. Wang, Y. Ding, E. Reed, R. D. Miller, and R. H. Dauskardt, Electrically conductive copper core–shell nanowires through benzenethiol-directed assembly, Nano Lett. **18**, 4900 (2018).

[11] R. J. Kashtiban, M. G. Burdanova, A. Vasylenko, J. Wynn, P. V. Medeiros, Q. Ramasse, A. J. Morris, D. Quigley, J. Lloyd-Hughes, and J. Sloan, Linear and helical cesium iodide atomic chains in ultranarrow single-walled carbon nanotubes: Impact on optical properties, ACS Nano **15**, 13389 (2021).

[12] A. A. Balandin, R. K. Lake, and T. T. Salguero, One-dimensional van der Waals materials—Advent of a new research field, Appl. Phys. Lett. **121**, 040401 (2022).

[13] Y. Meng, W. Wang, and J. C. Ho, One-dimensional atomic chains for ultimate-scaled electronics, ACS Nano **16**, 13314 (2022).

[14] M. A. Stolyarov, G. Liu, M. A. Bloodgood, E. Aytan, C. Jiang, R. Samnakay, T. T. Salguero, D. L. Nika, S. L. Rumyantsev,

M. S. Shur, *et al.*, Breakdown current density in h-BN-capped quasi-1D $TaSe_3$ metallic nanowires: Prospects of interconnect applications, Nanoscale **8**, 15774 (2016).

[15] A. Geremew, M. Bloodgood, E. Aytan, B. Woo, S. Corber, G. Liu, K. Bozhilov, T. Salguero, S. Rumyantsev, M. Rao, *et al.*, Current carrying capacity of quasi-1D $ZrTe_3$ van der Waals nanoribbons, IEEE Electron Device Lett. **39**, 735 (2018).

[16] J. O. Island, A. J. Molina-Mendoza, M. Barawi, R. Biele, E. Flores, J. M. Clamagirand, J. R. Ares, C. Sánchez, H. S. Van Der Zant, R. D'Agosta, *et al.*, Electronics and optoelectronics of quasi-1D layered transition metal trichalcogenides, 2D Mater. **4**, 022003 (2017).

[17] A. Lipatov, M. J. Loes, H. Lu, J. Dai, P. Patoka, N. S. Vorobeva, D. S. Muratov, G. Ulrich, B. Kästner, A. Hoehl, *et al.*, Quasi-1D TiS_3 nanoribbons: Mechanical exfoliation and thickness-dependent Raman spectroscopy, ACS Nano **12**, 12713 (2018).

[18] H. Pfnür, C. Tegenkamp, S. Sanna, E. Jeckelmann, M. H. von Hoegen, U. Bovensiepen, N. Esser, W. G. Schmidt, M. Dähne, S. Wippermann, F. Bechstedt, M. Bode, R. Claessen, R. Ernstorfer, C. Hogan, M. Ligges, A. Pucci, J. Schäfer, E. Speiser, M. Wolf, *et al.*, Atomic wires on substrates: Physics between one and two dimensions, Surf. Sci. Rep. **79**, 100629 (2024).

[19] L. Reining and R. Del Sole, Screened Coulomb interaction at Si (111) 2×1, Phys. Rev. B **44**, 12918 (1991).

[20] R. Saito, G. Dresselhaus, and M. S. Dresselhaus, *Physical Properties of Carbon Nanotubes* (Imperial College Press, London, 2001).

[21] C. D. Spataru, S. Ismail-Beigi, L. X. Benedict, and S. G. Louie, Excitonic effects and optical spectra of single-walled carbon nanotubes, Phys. Rev. Lett. **92**, 077402 (2004).

[22] F. Wang, D. J. Cho, B. Kessler, J. Deslippe, P. J. Schuck, S. G. Louie, A. Zettl, T. F. Heinz, and Y. R. Shen, Observation of excitons in one-dimensional metallic single-walled carbon nanotubes, Phys. Rev. Lett. **99**, 227401 (2007).

[23] J. Deslippe, M. Dipoppa, D. Prendergast, M. V. O. Moutinho, R. B. Capaz, and S. G. Louie, Electron-hole interaction in carbon nanotubes: Novel screening and exciton excitation spectra, Nano Lett. **9**, 1330 (2009).

[24] A. Tries, S. Osella, P. Zhang, F. Xu, C. Ramanan, M. Kläui, Y. Mai, D. Beljonne, and H. I. Wang, Experimental observation of strong exciton effects in graphene nanoribbons, Nano Lett. **20**, 2993 (2020).

[25] Cesar E. P. Villegas and A. R. Rocha, Screened hydrogen model of excitons in semiconducting nanoribbons, Phys. Rev. B **109**, 165425 (2024).

[26] G. Soavi, S. D. Conte, C. Manzoni, D. Viola, A. Narita, Y. Hu, X. Feng, U. Hohenester, E. Molinari, D. Prezzi, K. Müllen, and G. Cerullo, Exciton-exciton annihilation and biexciton stimulated emission in graphene nanoribbons, Nat. Commun. **7**, 11010 (2016).

[27] F. Bonabi, S. J. Brun, and T. G. Pedersen, Excitonic optical response of carbon chains confined in single-walled carbon nanotubes, Phys. Rev. B **96**, 155419 (2017).

[28] S. Kutrovskaya, S. Demirchyan, A. Osipov, S. Baryshev, A. Zasedatelev, P. Lagoudakis, and A. Kavokin, Exciton energy spectra in polyyne chains, Phys. Rev. Res. **3**, 013071 (2021).

[29] M. L. Tiago, M. Rohlfing, and S. G. Louie, Bound excitons and optical properties of bulk trans-polyacetylene, Phys. Rev. B **70**, 193204 (2004).

[30] J. S. Bola, R. M. Stolley, P. Poudel, J. S. Miller, C. Boheme, and Z. V. Vardeny, Influence of dark excitons on the electroabsorption spectrum of polyacetylene, Phys. Rev. B **110**, 075150 (2024).

[31] K. Nakayama, A. Tokuyama, K. Yamauchi, A. Moriya, T. Kato, K. Sugawara, S. Souma, M. Kitamura, K. Horiba, H. Kumigashira, T. Oguchi, T. Takahashi, K. Segawa, and T. Sato, Observation of edge states derived from topological helix chains, Nature (London) **631**, 54 (2024).

[32] V. V. Poborchii, A. V. Fokin, and A. A. Shklyaev, Optical properties of extreme tellurium nanowires formed in subnanometer-diameter channels, Nanoscale Adv. **5**, 220 (2023).

[33] S. Grillo, C. Cignarella, F. Bechstedt, P. Gori, M. Palummo, D. Campi, N. Marzari, and O. Pulci, Quasiparticle effects and strong excitonic features in exfoliable 1D semiconducting materials, ACS Nano **20**, 2664 (2026).

[34] T. Pham, S. Oh, P. Stetz, S. Onishi, C. Kisielowski, M. L. Cohen, and A. Zettl, Torsional instability in the single-chain limit of a transition metal trichalcogenide, Science **361**, 263 (2018).

[35] C. Shang, L. Fu, S. Zhou, and J. Zhao, Atomic wires of transition metal chalcogenides: A family of 1D materials for flexible electronics and spintronics, JACS Au **1**, 147 (2021).

[36] L. Fu, C. Shang, S. Zhou, Y. Guo, and J. Zhao, Transition metal halide nanowires: A family of one-dimensional multifunctional building blocks, Appl. Phys. Lett. **120**, 023103 (2022).

[37] Y. Zhao, H. Qu, J. Zhao, L. Kang, and S. Zhou, One-dimensional excitonic insulator of M_6Te_6 (M = Mo, W) atomic wires, Nano Lett. **25**, 1108 (2025).

[38] Y. Feng, T. Dong, J. Zhao, and S. Zhou, One-dimensional all-metal nanowires with strong excitonic effect, Phys. Rev. Mater. **9**, 104603 (2025).

[39] F. Bechstedt, *Many-Body Approach to Electronic Excitations. Concepts and Applications* (Springer-Verlag, Berlin, 2015).

[40] D. Sangalli, A. Ferretti, H. Miranda, C. Attaccalite, I. Marri, E. Cannuccia, P. Melo, M. Marsili, F. Paleari, A. Marrazzo, G. Prandini, P. Bonfá, M. O. Atambo, F. Affinito, M. Palummo, A. Molina-Sánchez, C. Hogan, M. Grüning, D. Varsano, and A. Marini, Many-body perturbation theory calculations using the Yambo code, J. Phys.: Condens. Matter **31**, 325902 (2019).

[41] P. Hohenberg and W. Kohn, Inhomogeneous electron gas, Phys. Rev. **136**, B864 (1964).

[42] W. Kohn and L. J. Sham, Self-consistent equations including exchange and correlation effects, Phys. Rev. **140**, A1133 (1965).

[43] P. Giannozzi, S. Baroni, N. Bonini, M. Calandra, R. Car, C. Cavazzoni, D. Ceresoli, G. L. Chiarotti, M. Cococcioni, I. Dabo, A. D. Corso, S. de Gironcoli, S. Fabris, G. Fratesi, R. Gebauer, U. Gerstmann, C. Gougoussis, A. Kokalj, M. Lazzeri, L. Martin-Samos, *et al.*, QUANTUM ESPRESSO: A modular and open-source software project for quantum simulations of materials, J. Phys.: Condens. Matter **21**, 395502 (2009).

[44] P. Giannozzi, O. Andreussi, T. Brumme, O. Bunau, M. B. Nardelli, M. Calandra, R. Car, C. Cavazzoni, D. Ceresoli, M. Cococcioni, N. Colonna, I. Carnimeo, A. D. Corso, S. de Gironcoli, P. Delugas, R. A. DiStasio, Jr., A. Ferretti, A. Floris,

G. Fratesi, G. Fugallo, *et al.*, Advanced capabilities for materials modelling with QUANTUM ESPRESSO, J. Phys.: Condens. Matter **29**, 465901 (2017).
[45] C. A. Rozzi, D. Varsano, A. Marini, Eberhard K. U. Gross, and A. Rubio, Exact Coulomb cutoff technique for supercell calculations, Phys. Rev. B **73**, 205119 (2006).
[46] I. Guilhon, M. Marques, L. K. Teles, M. Palummo, O. Pulci, S. Botti, and F. Bechstedt, Out-of-plane excitons in two-dimensional crystals, Phys. Rev. B **99**, 161201(R) (2019).
[47] G. Yang, J. Fan, and S.-P. Gao, Momentum and thickness dependent excitonic and plasmonic properties of 2D h-BN and MoS_2 restored from supercell calculations, Nanoscale Adv. **5**, 6990 (2023).
[48] C. Kittel, *Introduction to Solid State Physics*, 8th ed. (John Wiley and Sons Inc., New York, Chichester, 2005).
[49] N. S. Rytova, The screened potential of a point charge in a thin film, Moscow Univ. Phys. Bull. **3**, 18 (1967).
[50] L. V. Keldysh, Coulomb interaction in thin semiconductor and semimetal films, JETP Lett. **29**, 658 (1979).
[51] P. Cudazzo, I. V. Tokatly, and A. Rubio, Dielectric screening in two-dimensional insulators: Implications for excitonic and impurity states in graphane, Phys. Rev. B **84**, 085406 (2011).
[52] O. Pulci, M. Marsili, V. Garbuio, P. Gori, I. Kupchak, and F. Bechstedt, Excitons in two-dimensional sheets with honeycomb symmetry, Phys. Status Solidi B **252**, 72 (2015).
[53] M. V. Durnev and M. M. Glazov, Excitons and trions in two-dimensional semiconductors based on transition metal dichalcogenides, Phys. Usp. **61**, 825 (2018).
[54] J. Jackson, *Classical Electrodynamics* (John Wiley & Sons, Inc., New York, 1975).
[55] C. E. P. Villegas, A. Vasquez-Marcani, and A. R. Rocha, Static dielectric response and screening in solid state physics: Why dimensionality matters in dielectrics, Am. J. Phys. **92**, 360 (2024).
[56] M. Abramowitz and I. A. Stegun, *Handbook of Mathematical Functions* (National Bureau of Standards, Washington, DC, 1964).
[57] I. S. Gradshteyn and I. M. Ryzhik, *Table of Integrals, Series, and Products*, 8th ed., edited by D. Zwillinger and V. Moll (Academic Press, Amsterdam, 2015).
[58] I. N. Sneddon, *Mixed Boundary Value Problems in Potential Theory* (North-Holland Publishing Company, Amsterdam, 1966).
[59] M. Fixman, Variational method for classical polarizabilities, J. Chem. Phys. **75**, 4040 (1981).
[60] J. Berger, P. de Boeij, and R. van Leeuwen, A physical model for the longitudinal polarizabilities of polymer chains, J. Chem. Phys. **123**, 174910 (2005).
[61] M. A. Gusmão, Simple approximation for the Bethe-ansatz solution of the one-dimensional Fermi gas, Phys. Rev. B **35**, 1682 (1987).
[62] G. Sesti, D. Varsano, E. Molinari, and M. Rontani, Anomalous screening in narrow-gap carbon nanotubes, Phys. Rev. B **105**, 195404 (2022).
[63] K. A. Bulshevich, *11th International Symposium "Nanostructures: Physics and Technology," St. Petersburg (Russia)*, June 23-28 (Ioffe Institute, St. Petersburg, 2003).
[64] S. Das Sarma and E. H. Hwang, Collective modes of the massless Dirac plasma, Phys. Rev. Lett. **102**, 206412 (2009).
[65] F. Léonard and J. Tersoff, Dielectric response of semiconducting carbon nanotubes, Appl. Phys. Lett. **81**, 4835 (2002).
[66] J. van den Brink and G. A. Sawatzky, Non-conventional screening of the Coulomb interaction in low-dimensional and finite-size systems, Europhys. Lett. **50**, 447 (2000).
[67] S. Brazovskii and N. Kirova, Physical theory of excitons in conducting polymers, Chem. Soc. Rev. **39**, 2453 (2010).
[68] G. Grosso and G. P. Parravicini, *Solid State Physics* (Academic Press, Cambridge, 2003).
[69] R. Loudon, One-dimensional hydrogen atom, Proc. R. Soc. A **472**, 20150534 (2016).
[70] G. W. Bryant and A. J. Glick, Impurity states in doped transpolyacetylene, Phys. Rev. B **26**, 5855 (1982).
[71] G. Abramovici and Y. Avishai, The one-dimensional Coulomb problem, J. Phys. A: Math. Theor. **42**, 285302 (2009).
[72] S. Z. Rakhmanov, O. V. Karpova, D. R. Rakhimboeva, F. S. Khashimova, and D. Babajanov, Quantum dynamics of hydrogen-like atom in one-dimensional box with oscillating walls, Nanosyst.: Phys. Chem. Math. **6**, 767 (2015).
[73] M. Calçada, J. T. Lunardi, L. A. Manzoni, W. Monteiro, and M. Pereira, A distributional approach for the one-dimensional hydrogen atom, Front. Phys. **7**, 101 (2019).
[74] R. Loudon, One-dimensional hydrogen atom, Am. J. Phys. **27**, 649 (1959).
[75] J. P. Perdew, K. Burke, and M. Ernzerhof, Generalized gradient approximation made simple, Phys. Rev. Lett. **77**, 3865 (1996).
[76] C. Cignarella, D. Campi, and N. Marzari, Searching for the thinnest metallic wire, ACS Nano **18**, 16101 (2024).
[77] L. Matthes, O. Pulci, and F. Bechstedt, Influence of out-of-plane response on optical properties of two-dimensional materials: First principles approach, Phys. Rev. B **94**, 205408 (2016).
[78] B. Adolph, V. I. Gavrilenko, K. Tenelsen, F. Bechstedt, and R. Del Sole, Nonlocality and many-body effects in the optical properties of semiconductors, Phys. Rev. B **53**, 9797 (1996).
[79] F. Bechstedt, P. Gori, and O. Pulci, Beyond graphene: Clean, hydrogenated and halogenated silicene, germanene, stanene, and plumbene, Prog. Surf. Sci. **96**, 100615 (2021).
[80] T. Galvani, F. Paleari, H. P. C. Miranda, A. Molina-Sánchez, L. Wirtz, S. Latil, H. Amara, and F. Ducastelle, Excitons in boron nitride single layer, Phys. Rev. B **94**, 125303 (2016).
[81] M. S. Prete, D. Grassano, O. Pulci, I. Kupchak, V. Olevano, and F. Bechstedt, Giant excitonic absorption and emission in two-dimensional group-III nitrides, Sci. Rep. **10**, 10719 (2020).
[82] F. Grasselli, Variational approach to the soft-Coulomb potential in low-dimensional quantum systems, Am. J. Phys. **85**, 834 (2017).
[83] K. Sallai, S. Hack, S. Majorosi, and A. Czirják, One-dimensional model potentials optimized for the calculation of high-order-harmonic-generation spectra, Phys. Rev. A **110**, 063117 (2024).

Correction: A relevant reference was missing at publication and has been added as Ref. [76]. The third sentence of the second paragraph of Sec. IV A has been modified to cite the new reference.